

**Product Development Team  
for  
NEXRAD Enhancements**

**Quarterly Report – 2<sup>nd</sup> Quarter FY 02**

**02.6.2 Polarization and Frequency Diversity**

*Continue development of algorithms that utilize polarization data to detect regions and fields of hydrometeors and non-hydrometeors, particularly those that are hazardous to aviation operations.*

a) Current Efforts

**(NSSL):**

**1. Polarimetric upgrade of WSR-88D**

02.6.2.E1 Milestone: Incorporate and test dual polarization scheme that uses simultaneous transmission and reception of H and V signals on the research WSR-88D platform.

NSSL has completed integration of all microwave and radio frequency components for producing dual polarization signals. Further, capability to transmit horizontal H and receive both H and V components or to transmit simultaneous H,V components has been tested and circuits to switch between these two modes are in place. Integration of a custom-made frequency generator, the radar IF circuits, and the Sigmet processor has been completed. First sample data from a polarimetric WSR-88D have been collected on 19 March 2002. An example of data collected for the second observed event on 25 March 2002 is displayed in Fig. 1.

Semiquantitative examination of the data indicates potential for a significantly better performance than obtainable by the Cimarron radar. It appears that useful estimates polarimetric variables can be obtained with dwell times of about 60ms, which is compatible with the current dwell times of the WSR-88Ds. In regions of rain, the cross correlation between the H and V signals was very close to one. Hence the statistical errors of differential reflectivity and differential phase were well under control. Tests are underway to calibrate the polarimetric variables and determine their temporal stability.

Software was developed to capture the polarimetric variables of the Sigmet processor and put these on the local area network for further processing such as censoring data, computing the specific differential phase, applying the hydrom-

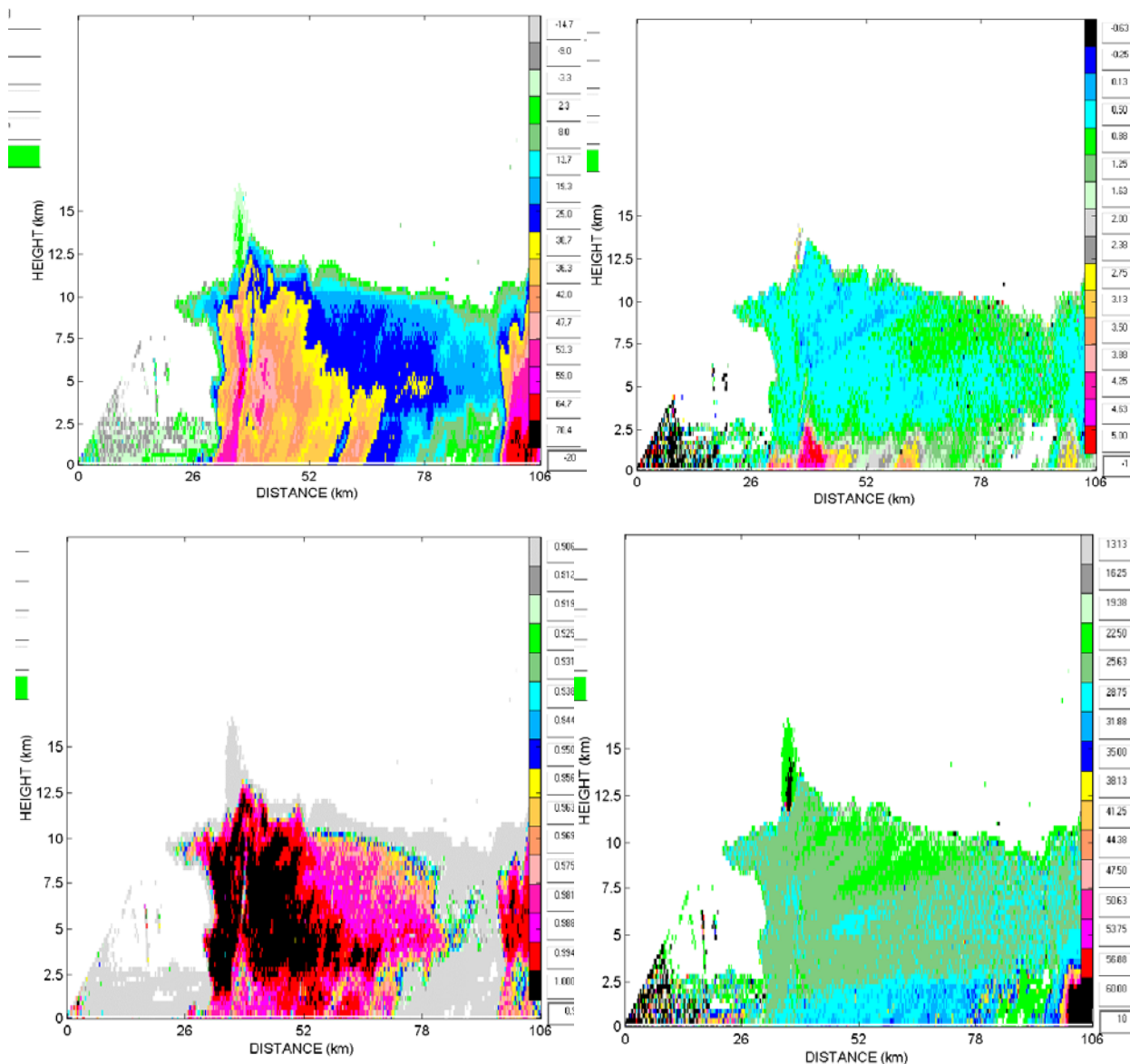


Figure 1. Composite RHI of radar reflectivity (left top), differential reflectivity (right top), cross-correlation coefficient (left bottom), and differential phase (right bottom) for a hail storm on 25 March 2002 observed with the KOUN radar (02:26 UTC). Az = 70.1°.

eteor classification scheme, and computing rainfall rates. These last two products will be supplied to the National Weather Service for evaluation.

## 2. Using weather data to calibrate polarimetric radars.

02.6.2.14 Refine a new radar hardware calibration technique using the consistency among polarimetric observations.

High-quality hydrometeor classification implies precise calibration of the measured polarimetric variables. Such radar parameters as Doppler velocity, differ-

ential phase, and cross-correlation coefficient do not require calibration, whereas radar reflectivity and differential reflectivity have to be calibrated. Accurate calibration of differential reflectivity  $Z_{DR}$  is especially important because this is most important parameter in the classification scheme. Discrimination between rain and snow as well as detection of icing impose particularly stringent requirements on the accuracy of the  $Z_{DR}$  measurements (0.1 - 0.2 dB). The problem is exacerbated if two receivers for orthogonal components of the radar echo are used instead of one (as in the scheme of simultaneous transmission for the WSR-88D radar) and if the radar beam experiences partial beam blockage at lower elevation angles.

NSSL has developed a technique to correct  $Z$  and  $Z_{DR}$  if both of these variables are corrupted due to system miscalibration and radar beam blockage. The technique is based on the idea of self-consistency among  $Z$ ,  $Z_{DR}$ , and  $K_{DP}$  (specific differential phase) for rain medium and polarization properties of dry snow and light rain. The suggested method capitalizes on the fact that  $K_{DP}$  is immune to the system miscalibration and partial beam blockage.

Our procedure was tested on the large data set collected by the NSSL's 11 cm Cimarron dual-polarization radar that experiences significant beam blockage at the elevation of  $0.5^\circ$ . Our results show that a polarimetric weather radar can be calibrated using such natural targets as rain and snow precipitation. This calibration can be performed for individual precipitation events in the process of data acquisition even if the radar beam is partially blocked. The accuracy of calibration is about 2 dB and 0.2 dB for  $Z$  and  $Z_{DR}$  respectively. It was found that the  $Z$  and  $Z_{DR}$  biases vary with azimuth due to partial obstruction of the radar beam by nearby trees and terrain profile. This azimuthal pattern didn't change significantly during at least four years of observations. No such modulation was observed at higher elevation ( $1.5^\circ$ ). Figures 2a and b illustrate stability of the

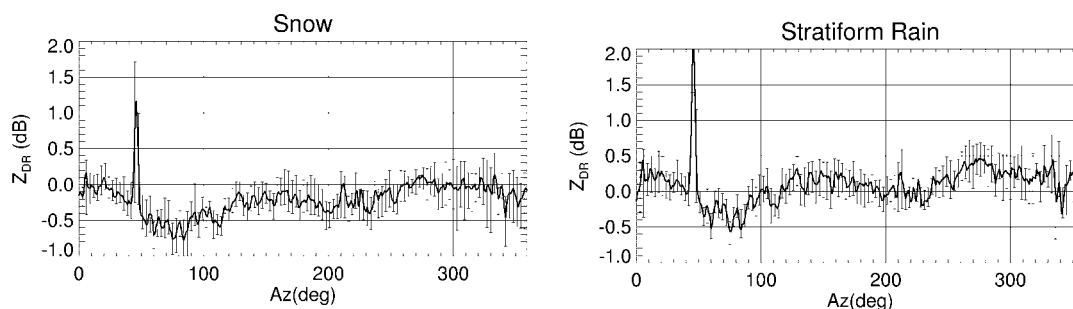


Figure 2. a) Mean azimuthal dependence of  $Z_{DR}$  for 7 snow events. Error bars indicate the range of  $Z_{DR}$  variations for all cases. b) Same as Fig. 2a but for 5 rain cases.

azimuthal pattern for the  $Z_{DR}$  bias estimated for several snow and light rain cases.

Figs. 2a and b show that the average difference between  $Z_{DR}$  in light rain and snow with the same radar reflectivity is about 0.3 dB. Therefore, the calibration accuracy of 0.2 dB for  $Z_{DR}$  that can be achieved with the proposed technique is sufficient to distinguish between snow and light rain.

### 3. Discrimination between light rain, freezing rain, and snow

Freezing rain is a dangerous phenomenon for all kinds of traffic and transportation including air traffic in the terminal area of airports. In order to assess the capability of a dual-polarization radar to identify freezing rain, we examined four recent winter events in Oklahoma. These include two cases of snow (11/28/01 and 02/05/02), one ordinary stratiform rain event (01/05/02), and one case of freezing rain (01/31/02) that resulted in approximately one hundred fifty million dollars damage in Oklahoma. Our analysis shows that the primary difference between these four storms is in differential reflectivity  $Z_{DR}$  and its dependence on radar reflectivity factor  $Z$ . Differential reflectivity is close to zero for aggregated snow near the ground regardless of its reflectivity, whereas  $Z_{DR}$  for rain is positive and increases with increasing  $Z$  (Fig. 3). Hence, reliable discrimination

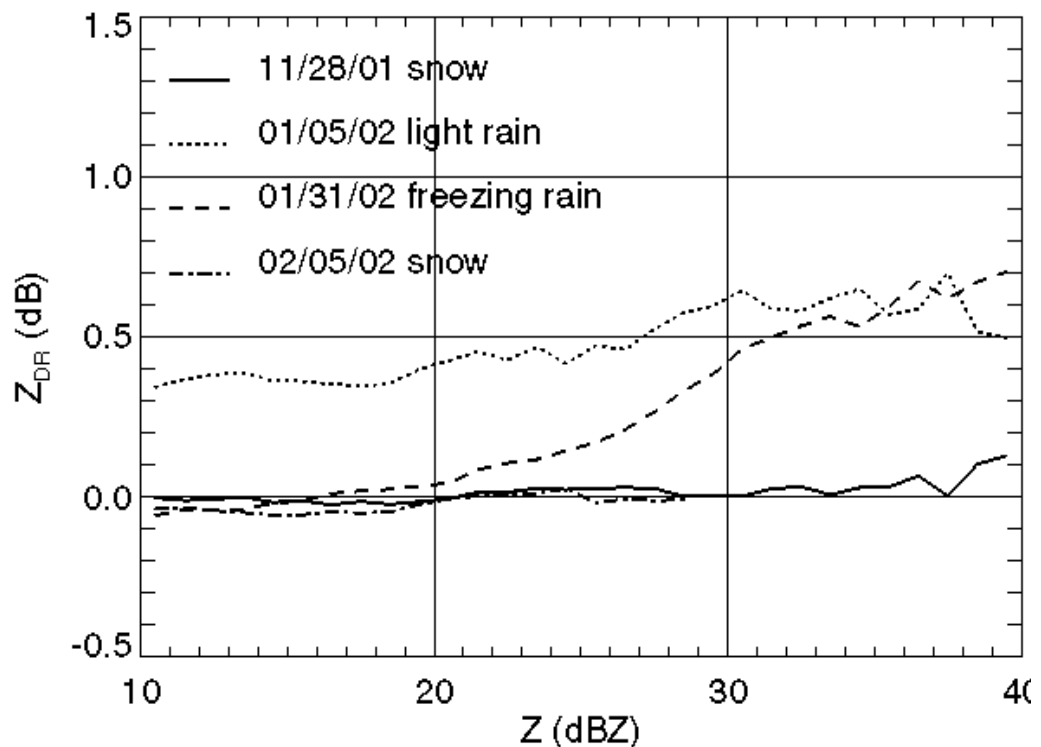


Figure 3. Average dependencies of  $Z_{DR}$  on  $Z$  for four winter events.

between rain and snow can be made only for reflectivities over 30 dBZ.

Although a dual-polarization radar enables discrimination between snow and rain, an analysis of surface temperature and sounding is necessary to delineate “ordinary rain” and freezing rain. Fig.5 illustrates typical vertical profiles of temperature for all four cases. The freezing rain event is characterized by a very strong temperature inversion aloft and by slightly negative surface temperatures. The sounding for this case (taken at Norman, OK, which was not hit by freezing rain) indicates the surface temperature about 0°C. In the zone of icing to the NW of Norman, surface temperatures were slightly negative (within the range from -3°C and -1°C). In contrast, no inversion was observed in

Although a dual-polarization radar enables discrimination between snow and rain, an analysis of surface temperature and sounding is necessary to delineate “ordinary rain” and freezing rain. Fig. 4 illustrates typical vertical profiles of tem-

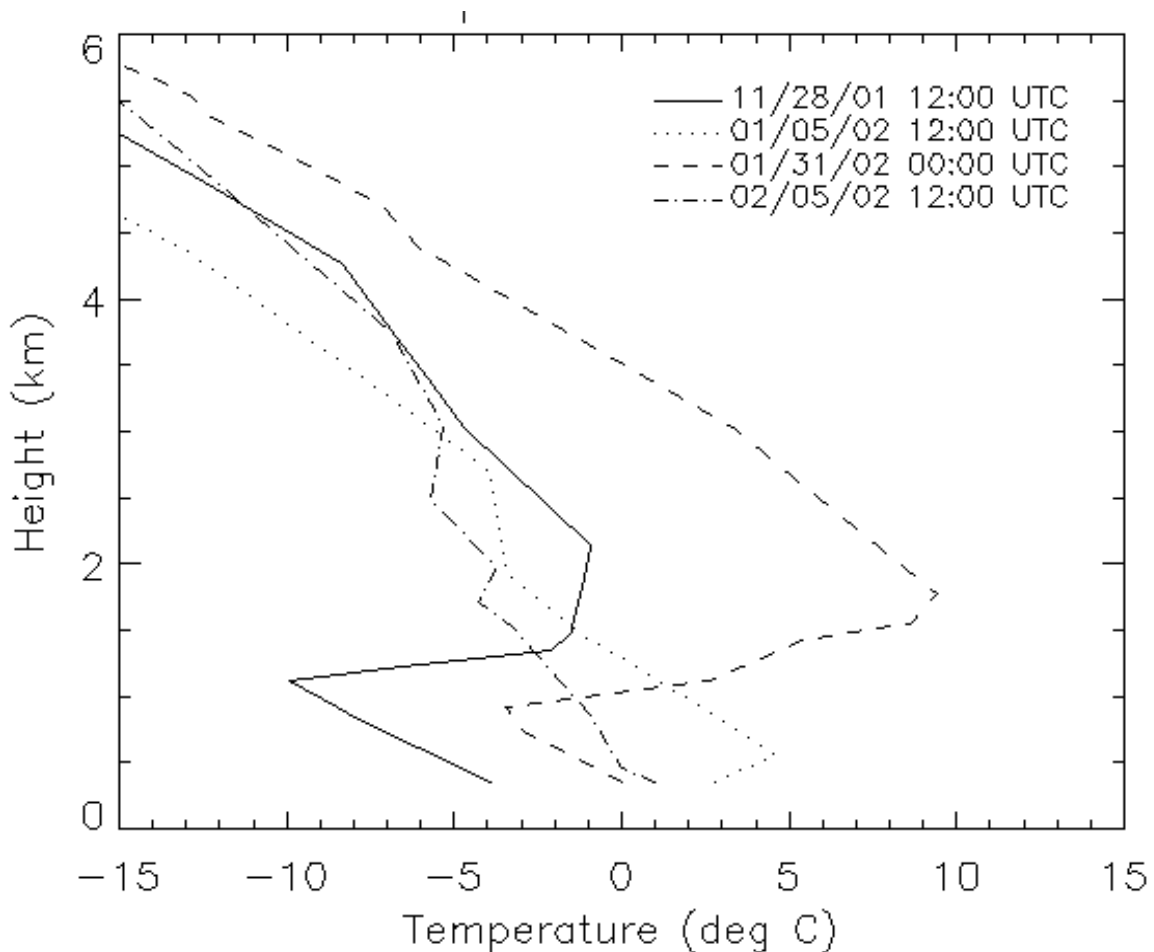


Figure 4. Vertical profiles of temperature for four winter events (Norman location).

perature for all four cases. The freezing rain event is characterized by a very strong temperature inversion aloft and by slightly negative surface temperatures. The sounding for this case (taken at Norman, OK, which was not hit by

freezing rain) indicates the surface temperature about 0°C. In the zone of icing to the NW of Norman, surface temperatures were slightly negative (within the range from -3°C and -1°C). In contrast, no inversion was observed in the snow case of 02/05/02 and the surface temperature was slightly positive.

#### **4. Discrimination between weather and sea clutter.**

Fuzzy logic classification method has been developed at NSSL to distinguish between weather echoes and sea clutter. The algorithm was tested on the data set obtained from the IMPROVE I Field Experiment: Offshore Frontal Precipitation Study conducted by the University of Washington west of the Seattle, WA, area during the period 4 January - 14 February 2001. The data were collected with the NCAR SPOL 10-cm dual-polarization radar located on the Pacific shoreline at the height of 10 m above sea level. The multiparameter data set includes backscattered power  $P$  (or radar reflectivity  $Z$ ), Doppler velocity  $V$ , spectrum width  $sv$ , differential reflectivity  $Z_{DR}$ , differential phase  $\Phi_{DP}$ , linear depolarization ratio  $LDR$ , and cross-correlation coefficient  $\rho_{hv}$ .

We consider two versions of classification scheme: polarimetric and non-polarimetric ones. The polarimetric classification algorithm utilizes  $SD(\Phi_{DP})$ ,  $\rho_{hv}$ ,  $LDR$ ,  $Z_{DR}$ ,  $V$ , and  $SD(P)$ , where  $SD(\Phi_{DP})$  and  $SD(P)$  are the standard deviations of  $\Phi_{DP}$  and  $P$  which characterize the texture of the  $\Phi_{DP}$  and  $P$  fields. Only  $SD(P)$  and  $V$  are used in the non-polarimetric version. Once discrimination between sea and weather clutter is made, a simple threshold of  $Z = -5$  dBZ is applied to distinguish between the marine boundary layer stratiform clouds (MBLSC) and convective precipitation.

Fig. 5 illustrates a case where sea clutter coexists with MBLSC and convective precipitation. MBLSC are denoted as “clouds”, whereas convective precipitation is marked as “precise”. As expected, the polarimetric algorithm exhibits superior performance. Although non-polarimetric version produces more speckles, it delineates quite well sea clutter and both types of weather echoes.

There are many NWS and FAA radars operating in the coastal regions of US. The standard technique for ground clutter rejection based on filtering around zero Doppler frequency doesn't work for sea clutter because the latter has essentially non-zero mean Doppler velocity. This study provides an alternate approach for sea clutter detection and rejection.

#### **(NCAR):**

- 1) A study of radar calibration using the consistency among polarimetric variables (reflectivity, differential reflectivity, and differential propagation phase)

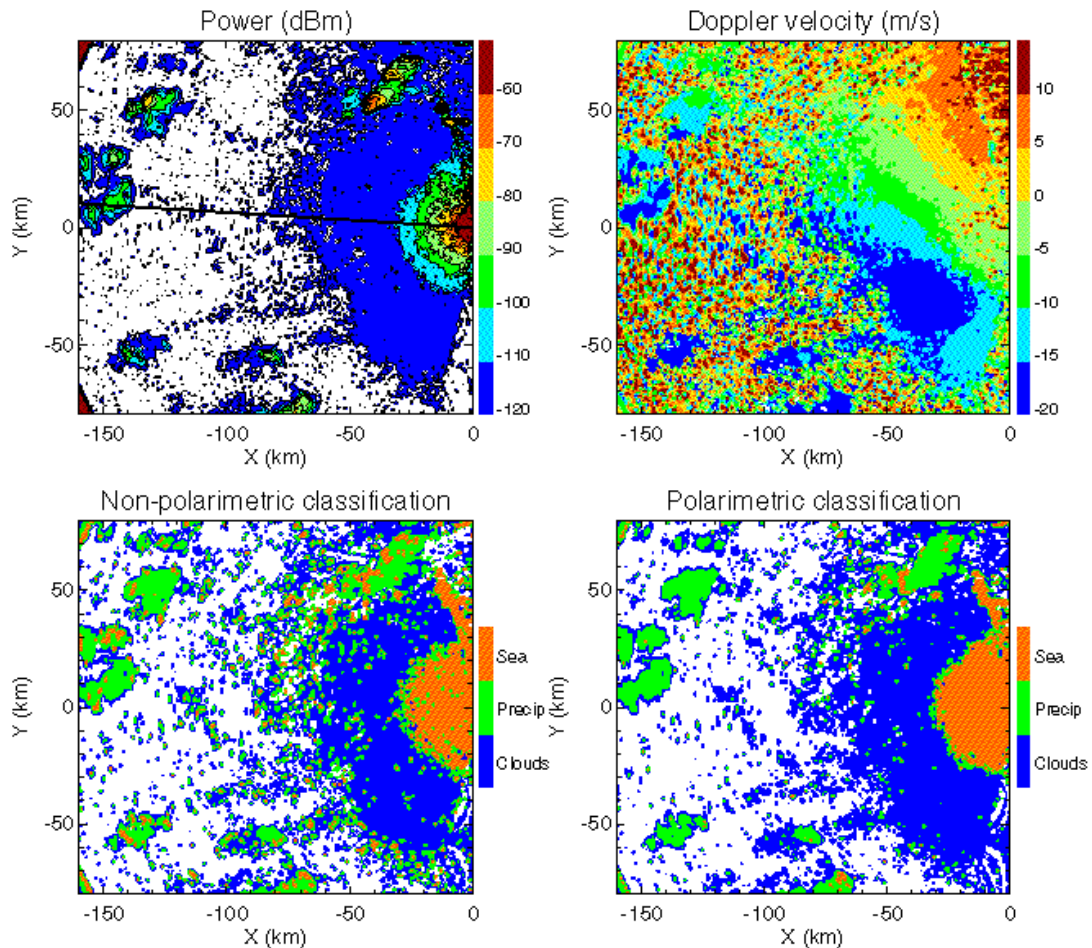


Figure 5. Combined plot of the fields of returned power  $P$ , mean Doppler velocity  $V$ , and results of non-polarimetric and polarimetric classification for data at  $0.0^\circ$  elevation on 2 February 2002 (16:10 UTC). The NCAR SPOL radar is located at (0,0).

was completed. A seminar on the results entitled “Polarization radar reflectivity calibration” was presented by J. Vivekanandan on 19 March. The abstract reads:

“Accurate calibration of radar reflectivity is essential for obtaining reliable rain rate estimation. For example, a 1 dB bias in reflectivity produces an 18% bias in radar-based rain rate estimation. A novel method of calibrating radar reflectivity using polarization radar measurements in rain is described. The differential propagation phase is unaffected by absolute calibration of the radar system. This parameter can be estimated from the power measurements and compared to the measured phase. Differences are indicative of calibration bias. Polarization measurements are sensitive to the drop size distribution (DSD) and mean drop shape. It is important to devise a calibration technique that is unperturbed by changes in DSD and drop shape. The proposed method is applied for calibrating reflectivity measurements of the NCAR (National Center for Atmo-

spheric Research) S-Pol (S-band polarization radar) in mid-latitude, sub-tropical and tropical rain events.”

2) Analysis of the rain-snow event of 18 February 1997 continued. This work is described, in part, in a paper to be presented at the 10th Conference on Aviation, Range, and Aerospace Meteorology. A copy of the paper was sent last month. Rain-snow designations are sensitive to the height of the freezing level. The difficulty in rain-changing-to-snow cases is that the 0C height can be close to ground, vertical, or below the surface. The 18 February event is also being used to refine the freezing level designation algorithm.

3) Analysis of polarimetric radar measurements obtained during snow events observed on 1 and 8 March is in progress. The data are being used for rain-snow discrimination and an attempt to improve the quantitative estimate of liquid equivalents with radar. The data set for 8 March includes snow particle type observations that are being used for verification of the hydrometeor classification algorithm.

4) A paper describing a procedure to retrieve the governing parameters of drop-size distributions was prepared for the 11th Conference on Cloud Physics (attached as a PDF document, Appendix A). This activity is funded largely by the U.S. Weather Research Program but is closely tied to the hydrometeor classification algorithm effort.

5) The interactive procedure for evaluating the weights of each radar parameter in hydrometeor classifications is undergoing testing and refinement. The procedure yields the input parameters, membership function values, and summations for each designation category. It permits interrogation of individual HCA designations and lists other possible designations based on total weights.

#### b) Planned Efforts

NSSL: Continue development of improved techniques.

NCAR:

#### d) Interface with other Organizations

None.

#### e) Activity Schedule Changes

Task 02.6.3 (Use of confidence factors to enhance separation of hydrometeors classes) has been superseded by task 02.6.15 (Discrimination between sea clutter, marine stratocumulus clouds and precipitation using conventional and dual-polarization Doppler radars).



### **02.6.3 Circulations**

*Display the NSSL Mesocyclone Detection Algorithm (MDA) and Tornado Detection Algorithm (TDA) output to Corridor Integrated Weather System users to establish utility for Terminal Convective Weather Forecast (TCWF) and National Convective Weather Forecast (NCWF) aviation users.*

#### a) Current Efforts

No progress to report. Task is set to begin 01 Aug 02.

#### b) Planned Efforts

To begin 01 Aug 02.

#### c) Problems/Issues

None.

#### d) Interface with other Organizations

None.

#### e) Activity Schedule Changes

None.

### **02.6.4 Technical Facilitation**

*Continue to develop software infrastructure and tools required for the development and testing and display of NEPDT algorithms.*

#### a) Current Efforts

The WDSS2 system was enhanced in several ways to support various research efforts at NSSL, to implement new visualization techniques and to access new types of data.

1) 3D lightning data can now be accessed and visualized (Fig. 6).

2) A process that merges data from different sensors in real-time was implemented.

3) Work has begun on ingesting near-storm environment data, derived from the RUC model, into WDSS-II.

4) Real-time ingest of mesonet data has now been implemented (Fig. 7)

5) NewVolume and NewElevation events are now supported for all radar data formats. These events were required for current algorithms such as SSAP.

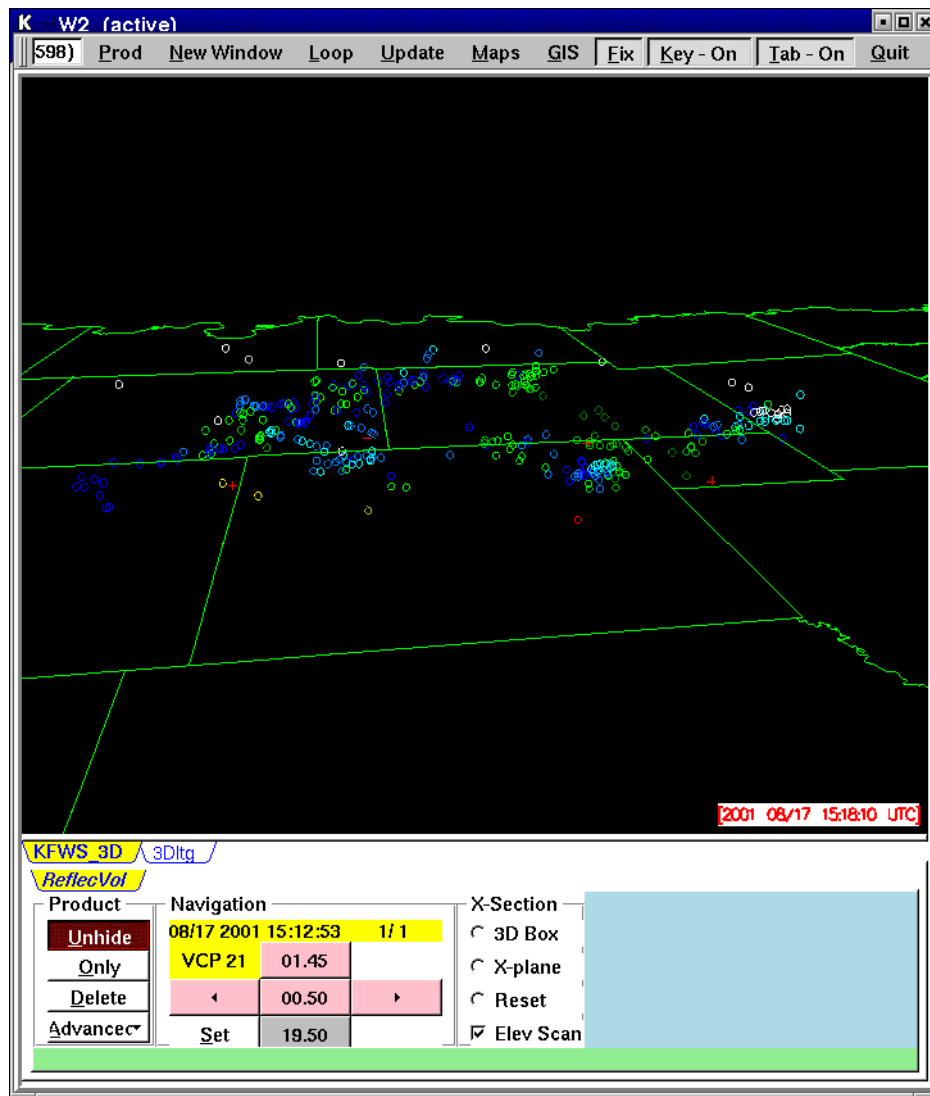


Figure 6. Screen shot of 3D lightning. The image shows the path of a single lightning strike in a thunderstorm on Aug. 17, 2001 near Fort Worth. The red plus is the point of contact with the ground. The other parts of the lightning strike are color-coded based on height, with hotter colors closer to the earth. This visualization is purely proof-of-concept, and better visualization is being developed in collaboration with lightning researchers at NSSL.

6) Completed implementation of a LDM Level-II radar format reader for interfacing with the CRAFT project. Thus, weather radar data from multiple sensors can be distributed via LDM and accessed by WDSS-II algorithms and displays (Fig. 8)..

7) We defined and implemented a LDM method of distributing TDWR data as well. TDWR data can be accessed and visualized in WDSS-II (Figs. 9 and 10).

8) A north-pointing compass centered in the window was added to the display to aid navigation in 3D.

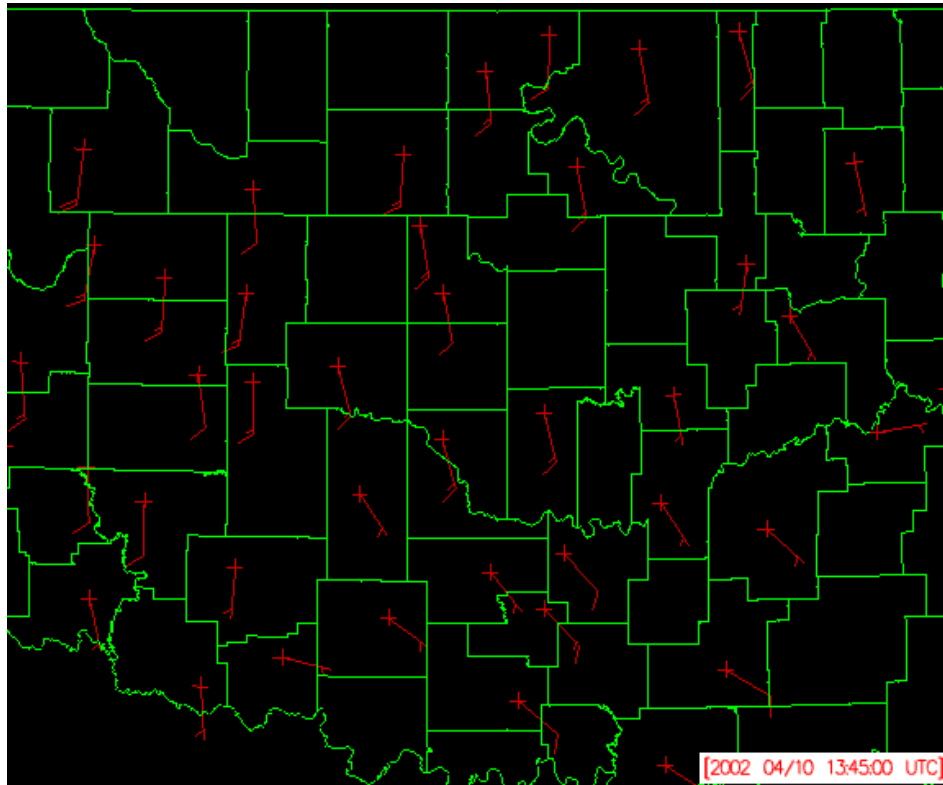


Figure 7. Oklahoma Mesonet wind data displayed within WDSS-II. Half barbs represent  $2.5 \text{ m s}^{-1}$  winds, while full barbs represent  $5 \text{ m s}^{-1}$  winds.

9) A GIS query interface was implemented, to provide a table of all algorithm detections and GIS products within a certain distance (or closest to) a user's query location (Fig. 11).

10) Virtual volume capability for all netcdf products, including those from LDM (Level-II and TDWR) was implemented.

11) Advanced GIS queries based on shapefile (map) information, rather than just on location, is being implemented.

12) Color maps can now be piece-wise linear, allowing for display of fine-grained detail. Shown is an example, digital terrain image (Fig. 12).

13) The K-Means clustering algorithm can now display clusters at various scales. This capability is supported by the WDSS-II display (Figs. 13, 14 and 15).

14) Added capability to display non-geographic drawables such as labels, color keys, etc., things that are not physically tied to the Earth's surface.

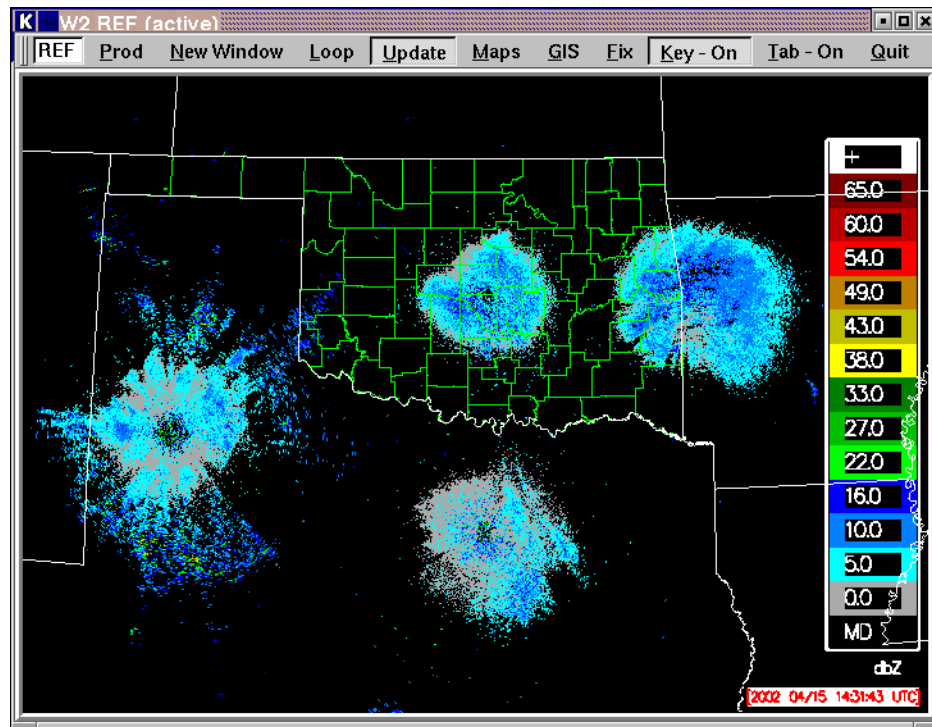


Figure 8. Data from several radars are shown superimposed on the earth's surface in a multi-sensor view. Shown are radars at Oklahoma City, Fort Smith, Fort Worth and Lubbock. Also on-line from the same region (but not shown) are radars at Amarillo and Tulsa.

b) Planned Efforts

Continue display interface and capability development and enhancement.

c) Problems/Issues

None.

d) Interface with other Organizations

None.

e) Activity Schedule Changes

None.

**02.6.9 Composite Products**

*Composite Products - develop a high-resolution multi-radar product with nested resolutions from 500 m to 5 km, that runs in a large analysis domain (such as CIWS), and that is updated at no more than 240 s intervals.*

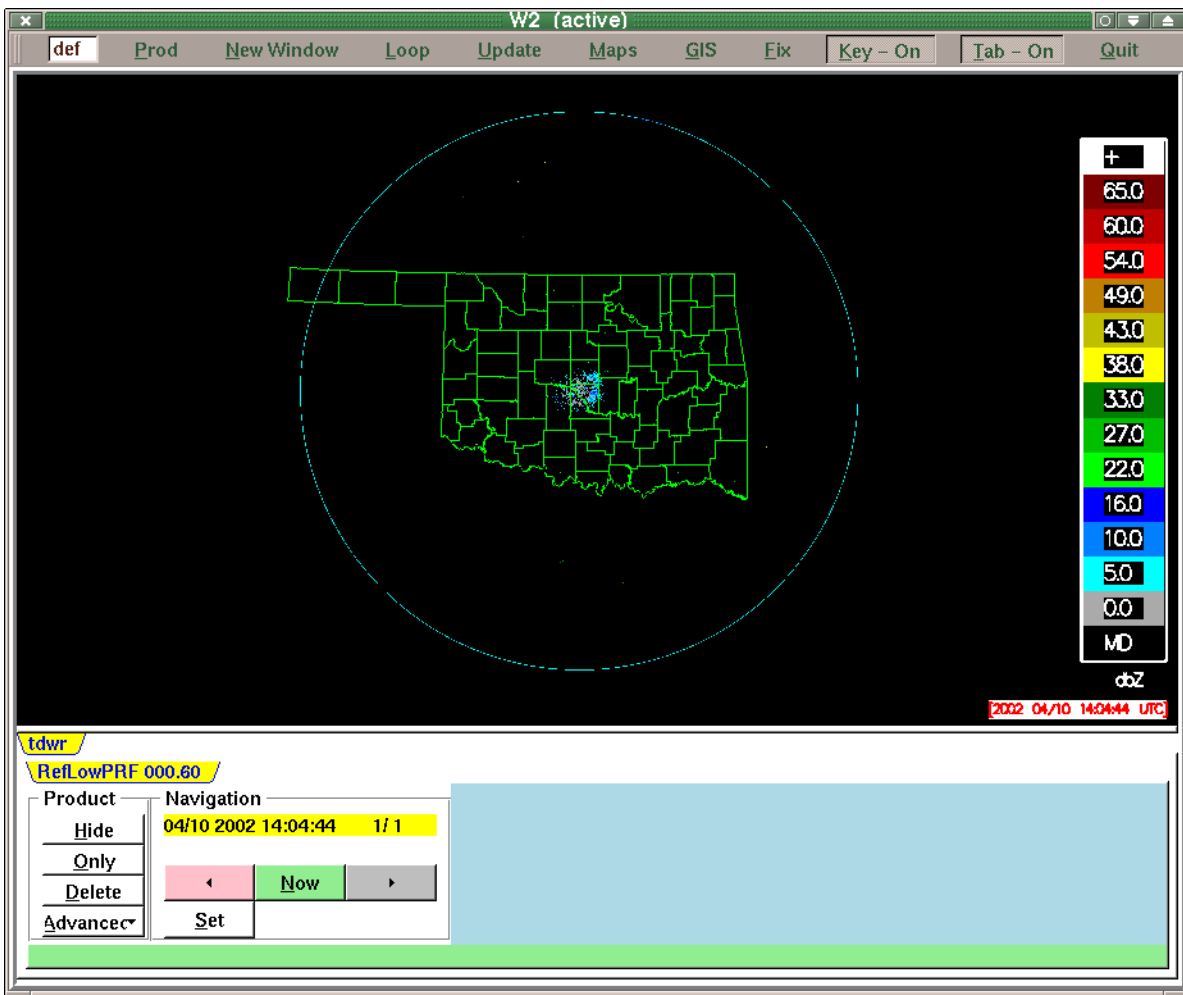


Figure 9. Reflectivity low PRF and signal to noise ratio images collected in real-time from TDWR data that are distributed via LDM.

#### a) Current Efforts

Collected real-time example data from the Oklahoma City International Airport (OKC) TDWR (Terminal Doppler Weather Radar). Obtained the TWDR data decoder software and began to decode the TDWR data format.

#### b) Planned Efforts

Begin to convert TDWR data into an internal binary format (for running 3-D multi-radar mosaic) and into a common format (e.g., network Common Data Form, or, NetCDF). Test BBID (bright-band identification) scheme on the TDWR and WSR-88D data.

#### c) Problems/Issues

None.

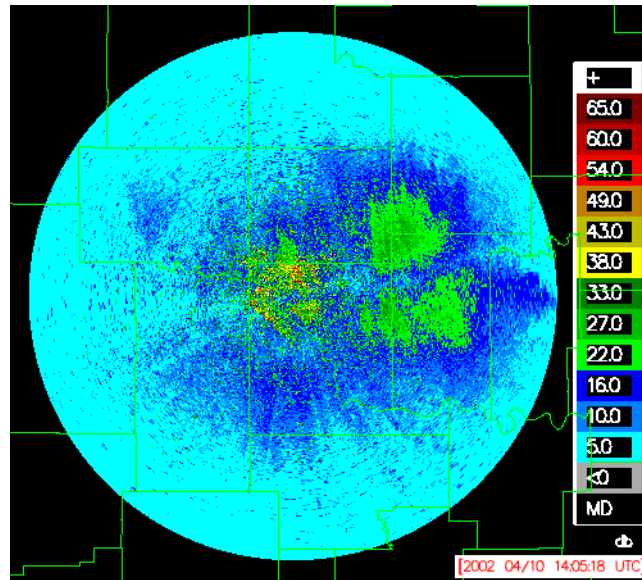


Figure 10. Signal to noise ratio for a high PRF TDWR scan, obtained via LDM ingest into WDSS-II.

-606.42136 -5118.74196 3759.67204				
Row Name	Distance	Attribute	Value	Unit
80	7.123	HgtMXZ	1.7	Kilometers
52	8.363	LtngRate	missing	dimensionless
96	14.362	MXConv	0	MetersPerSecond
62	15.470	MXZ	56	dimensionless
		Mass	480	Kilograms
		NegLtng	missing	dimensionless
		POH	40%	%
		PctPosLtng	missing	%
		Range	59.6	NauticalMiles
		RefIRatio	100	%
		RowName	52	dimensionless
		SRH	missing	SquareMetersPerSquareSecond
		SVRH	0%	%
		Speed	42.8	Knots
		ThrDLtng	missing	dimensionless
		Top	24.6	Kilofeet
		VIL	23	KilogramsPerSquareMeter

Figure 11. The result of an example query shows the nearest four storms to the cursor point on the earth's location. This is a multiple algorithm/multiple sensor query, and information corresponding to all storms may be obtained.

#### d) Interface with other Organizations

None.

#### e) Activity Schedule Changes

None.

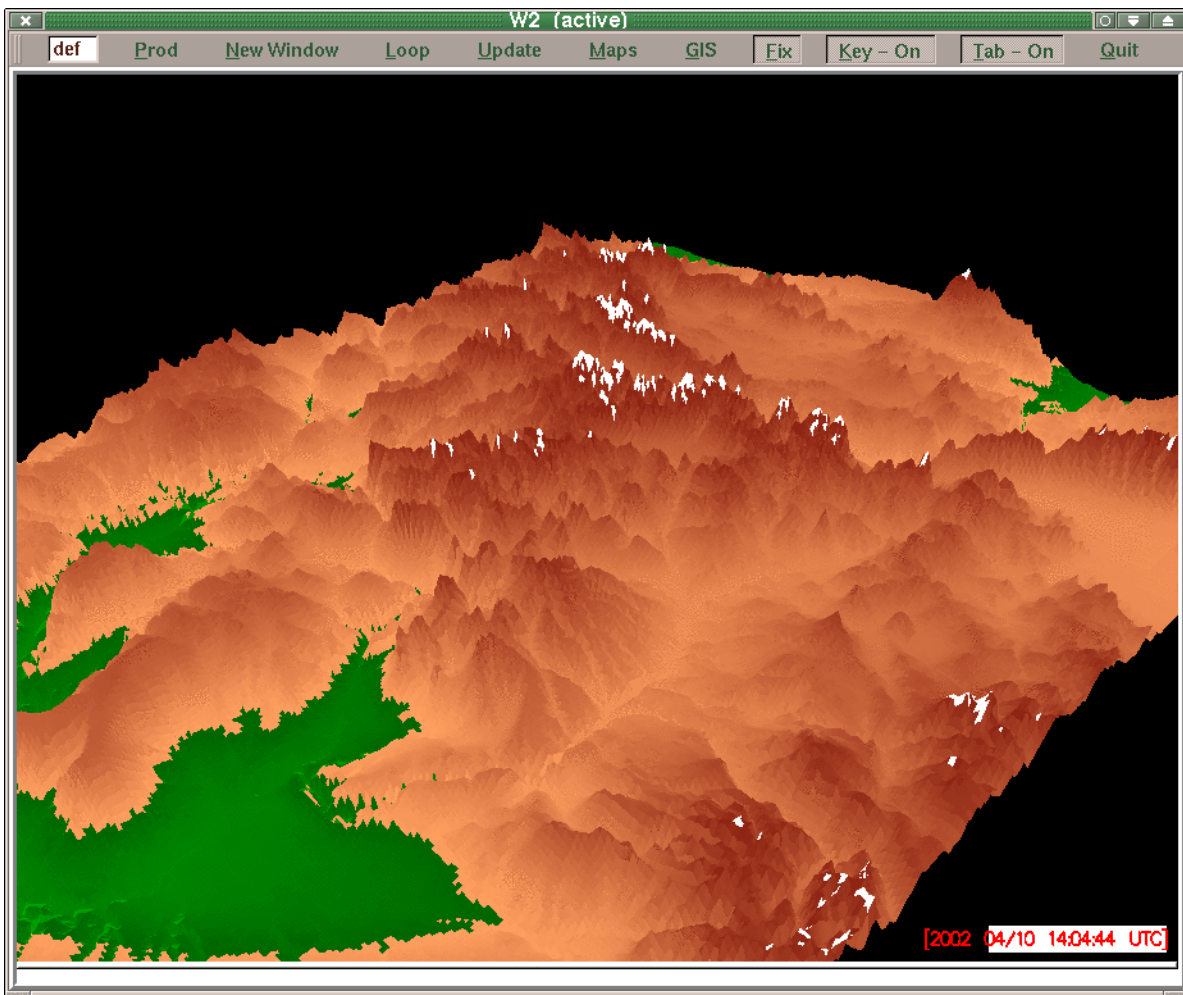


Figure 12. A digital terrain image that can be used to gauge the distance from ground of radar data.

#### **02.6.11 Volume Coverage Patterns**

*Volume Coverage Patterns - develop and implement new VCPs to meet the WSR-88D coverage needs of the aviation community and the AWR PDTs.*

##### a) Current Efforts

During this quarter, new VCP data were collected on the following dates:

01/29/02 - 01/31/02 Rain/freezing rain event

02/04/02 - 02/05/02 Winter weather event

##### b) Planned Efforts

Continue analysis and data collection on new VCP's. In particular, check that current algorithms are compatible with new VCP's, and correct any incompatibilities.

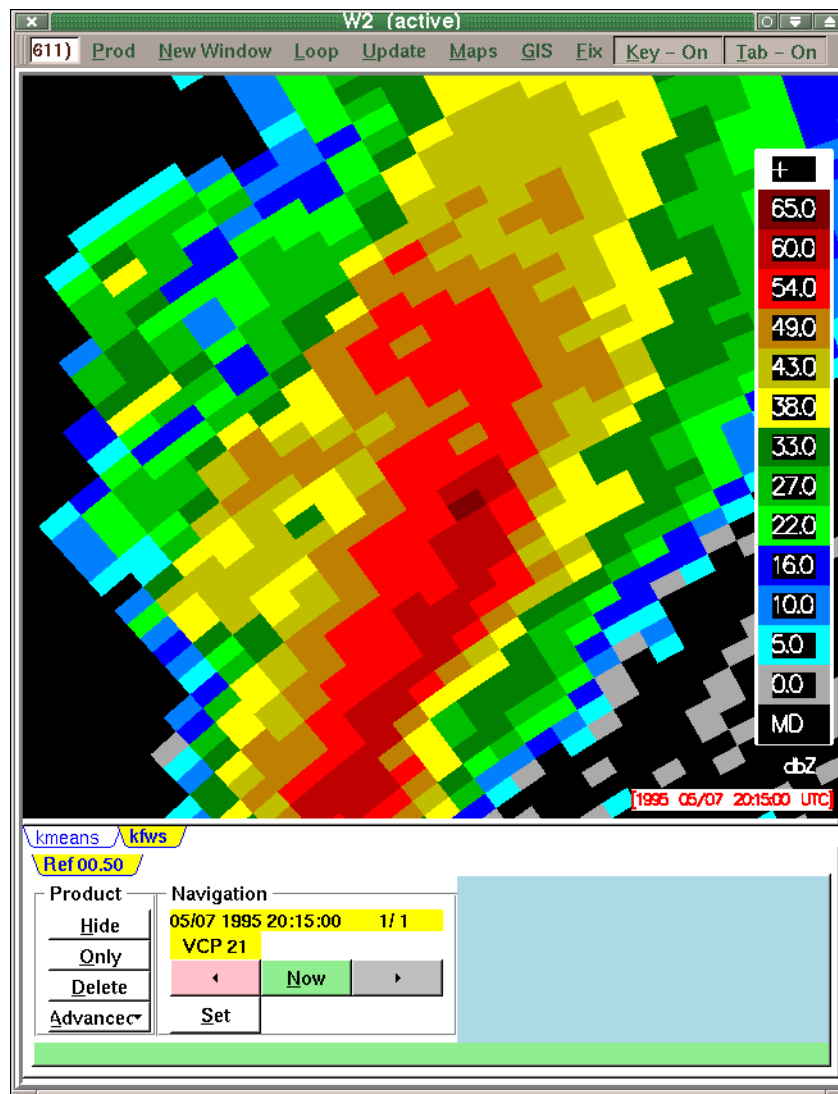


Figure 13. Raw radar data on which the K-Means clustering algorithm is applied.

c) Problems/Issues

None.

d) Interface with other Organizations

None.

e) Activity Schedule Changes

None



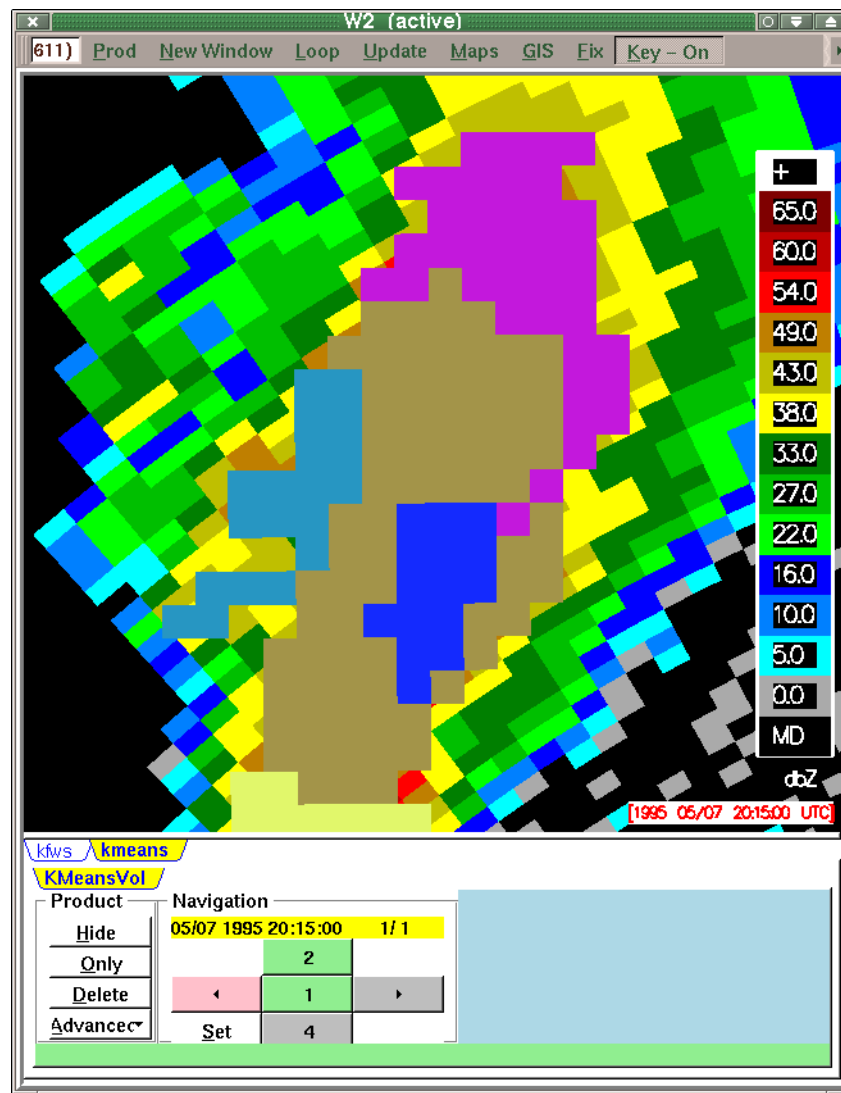


Figure 14. Solid color regions (blue, magenta, brown and cyan) show the most detailed (or, alternatively, the least distinct) clusters found by the K-means algorithm, overlaid on the raw radar data.

## 02.6.12 Product Implementation

*Explore and define aviation-specific products and implementation paths appropriate for NEPDT efforts.*

### a) Current Efforts

New sea clutter rejection product development begun applicable to both polarimetric and non-polarimetric radars.

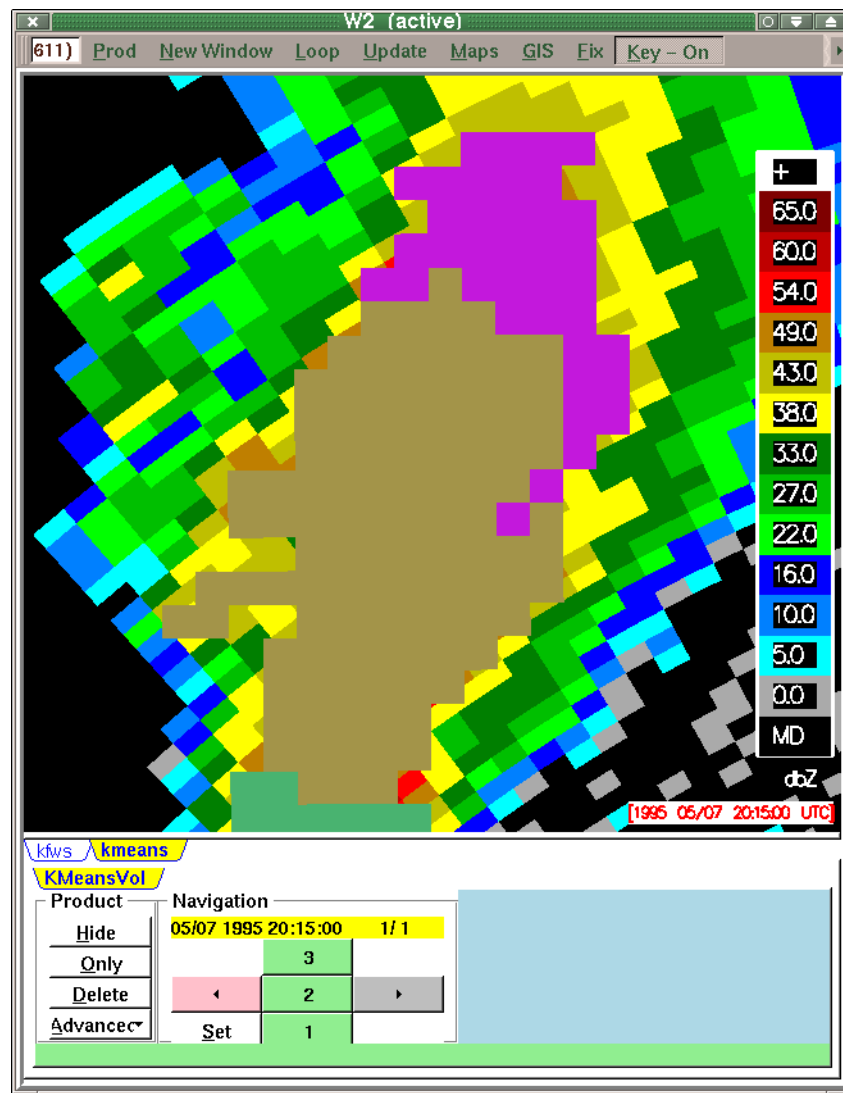


Figure 15. Clusters as in Fig. 13, but at the next level of distinction. Note that there are fewer clusters overall. As clusters become more distinct, the information associated with them becomes less detailed.

#### b) Planned Efforts

Continue exploring current product applications and new product development specific to aviation needs.

#### c) Problems/Issues

None.

#### d) Interface with other Organizations

None.

#### e) Activity Schedule Changes

None

### **02.6.14 Multi-radar Composites**

*Examine aspects of multiple radar integration and algorithms.*

#### a) Current Efforts

**02.6.14.1 FINAL REPORT.** The activities for the current quarter include selecting three wide spread precipitation volume scans, one in VCP 11 (from KTLX, Oklahoma) and two in VCP 21 (from KTLX and KRAX, North Carolina) for the 3D mosaic CPU benchmark testing. Figs.16a-c show composite reflectivity

**Table 1. 1 Technical specifics of the computer used for CPU testing.**

Computer model	Dell PowerEdge 6400
Operating System	Red Hat linux 7.1
CPU	4 x Pentium III Xeon processors (700 MHz)
Cache	1 MB per processor
RAM	512 MB per processor

fields for the three cases. Three gridding techniques, i.e., 1) radar bin volume mapping, 2) standard gap filling, and 3) advanced gap filling were tested using the benchmark cases. The computer used for the tests was a DELL PowerEdge 6400 server. Technical specifics of the computer are shown in Table 1. The three different gridding techniques and the associated results are presented below. Here “gridding” refers to the interpolation of radar reflectivity fields from 3-D radar spherical coordinates (i.e., r-range, j-azimuth, and q-elevation angle) onto a 3-D Cartesian grid (i.e., x-longitude, y-latitude, and z-height).

#### i) Radar Bin Volume Mapping.

The radar bin volume mapping is to fill in all Cartesian grid cells that are located within a given radar bin volume (size of 1 km  $\times$  1° $\times$  1° in the spherical coordinates) with the observed reflectivity value in the associated radar bin. There is no interpolation or smoothing in this process. The remapped fields simply show the original data distribution. Fig. 17 shows example images of the interpolated reflectivity fields using the bin volume mapping technique. There are two problems with the radar bin volume mapping: 1) data gaps/holes exist between the high tilts, especially for VCP 21 (Figs. 17a, 17b, and 17c); and 2) there are ring-shaped discontinuities on horizontal cross sections (Figs. 17a, 17b, and 17c).

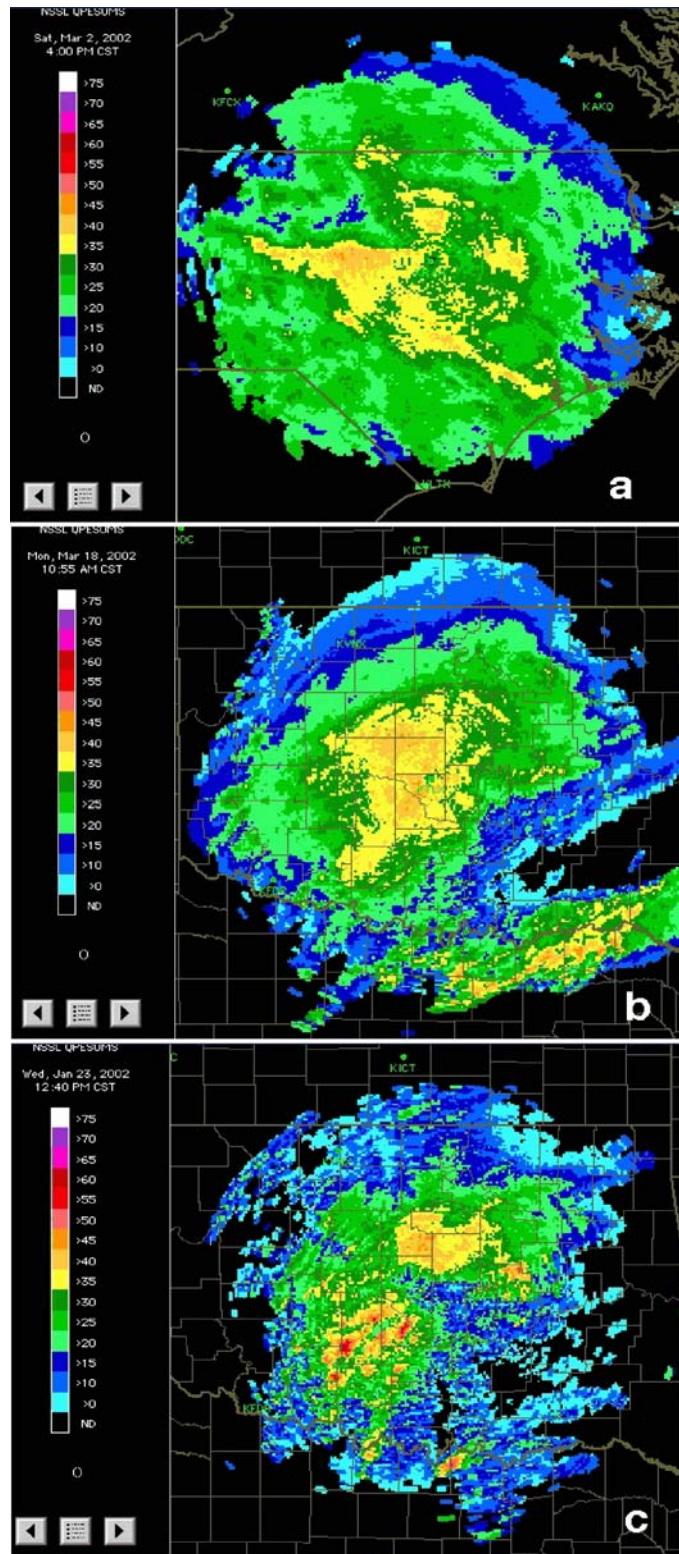


Figure 16. Composite reflectivities for the cases “NC 1” (panel a; time: 22Z March 2, 2002, location: North Carolina), “OK 1” (panel b; time: 1655Z March 18, 2002) and “OK 2” (panel c; time: 1840Z Jan. 23, 2002).

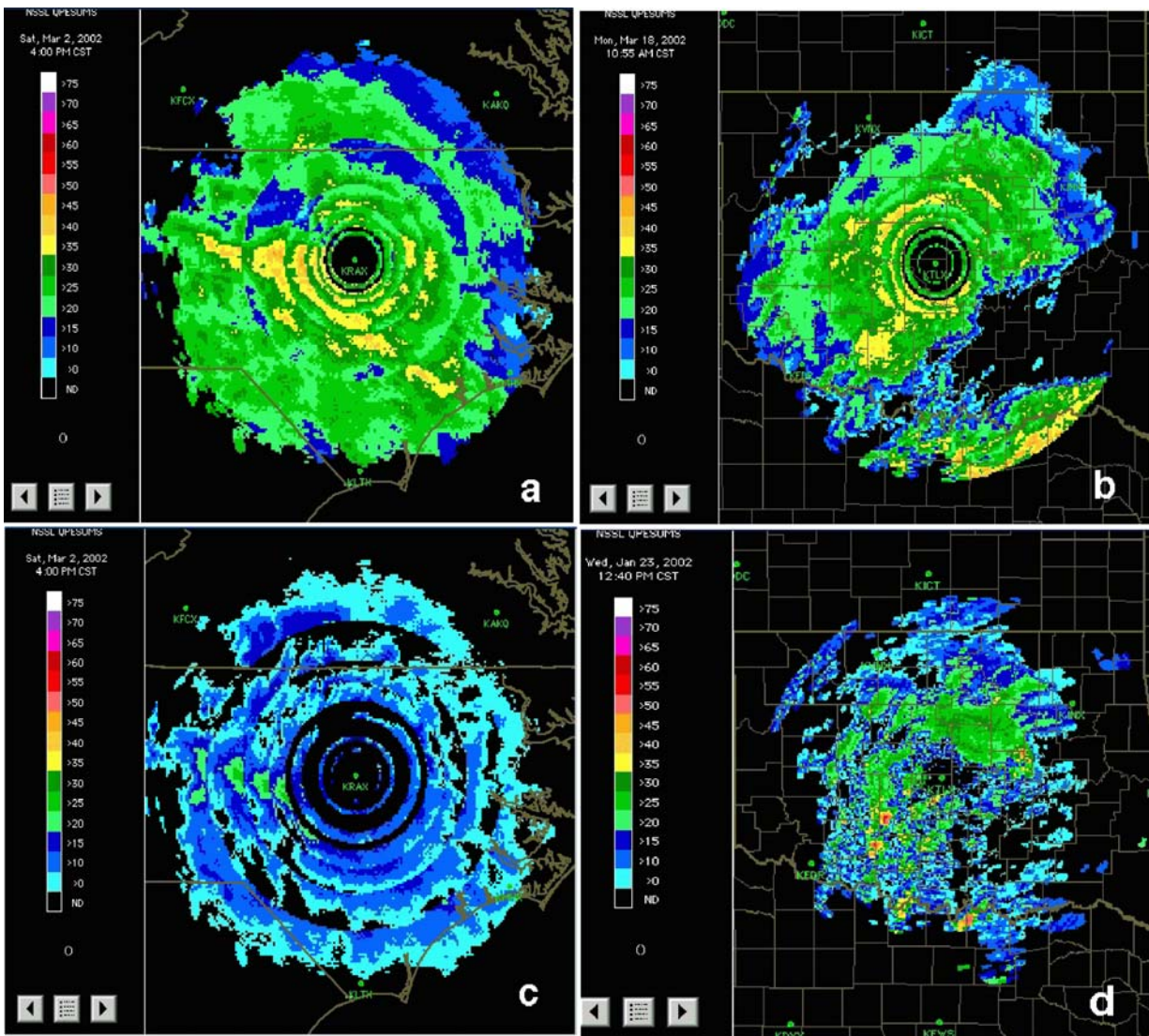


Figure 17. Horizontal cross sections of interpolated reflectivity field using the radar bin volume mapping. Panel a: case NC\_1; height = 2.5 km msl. Panel b: case OK 1; height = 3.5 km msl. Panel c: case NC 1, height = 6 km msl. Panel d: case OK 2; height = 4 km msl.

The first problem was due to that the higher tilts in both VCP 21 and VCP 11 are more than  $1^\circ$  apart (see Table 2). So when the radius of influence in elevation

**Table 2. Elevation angles (in degrees) for the 5th and higher tilts in VCP 11 and VCP 21.**

Tilt	5	6	7	8	9	10	11	12	13	14
VCP 11	4.3°	5.2°	6.2°	7.5°	8.7°	10.0°	12.0°	14.0°	16.7°	19.5°
VCP 21	4.3°	6.0°	9.9°	14.6°	19.5°	NA	NA	NA	NA	NA

angle direction is  $1^\circ$ , there will be voids shown between the higher tilts. This



problem will be addressed by the standard gap filling and the advanced gap-filling techniques (see sections b and c below).

The second problem was due to the poor radar sampling in regions where there are strong vertical reflectivity gradients (e.g., near a bright band or echo top). Figs. 18 and 19 illustrate this sampling problem using a simplified vertical

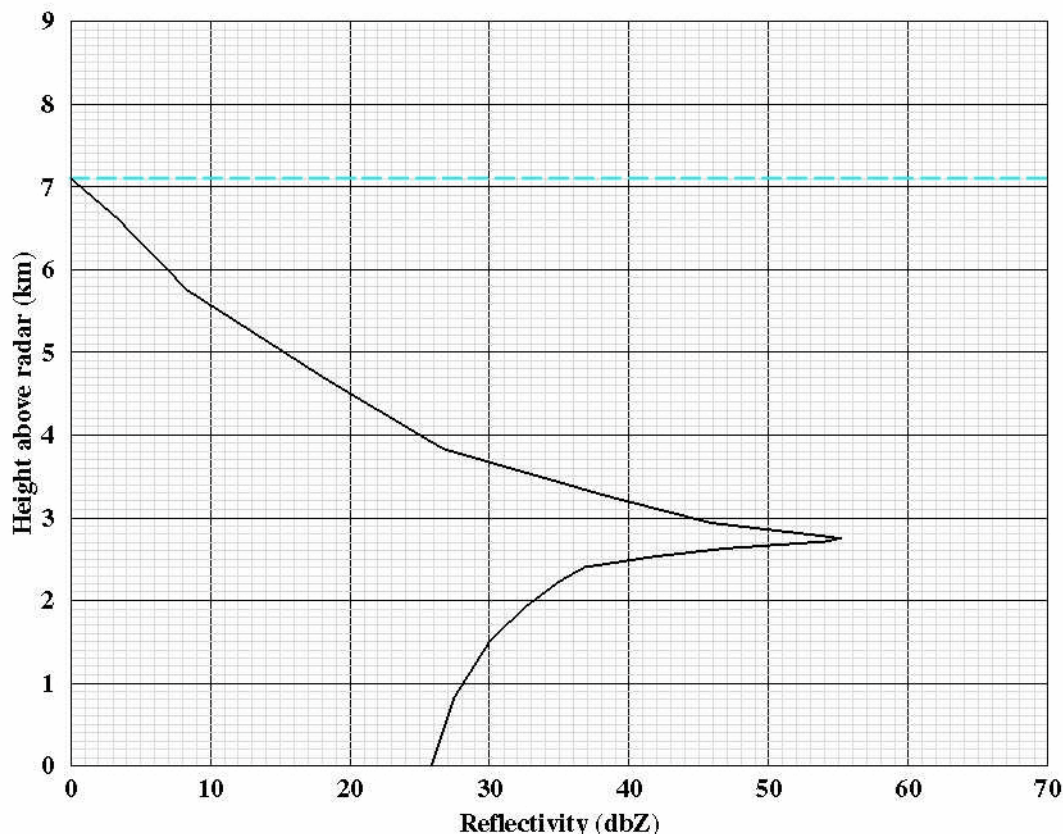


Figure 18. 3 An example vertical reflectivity profile. The blue dashed line represents the cloud top.

reflectivity profile. The profile assumes a bright band located around 2.75 km above the radar level and an echo top at about 7 km (Fig. 18). At the height of 3.5 km above radar, grid point A1 and A4 (Fig. 19a) are collocated with centers of radar bins P1 and P4, respectively, so they get reflectivity values of ~35 dbZ when using a bin volume mapping scheme. Grid points A2 and A3 are inside the radar bins P2 and P3 (Fig. 19a) so that they get values of ~22 and 55 dbZ, respectively. This is because that the center of radar bin P3 is located in the bright band and the reflectivity is high in the bright band. On the other hand, the center of radar bin P2 is located at a much higher altitude (4.2 km above the radar) than is the bin P3 so its reflectivity value is much lower according to the reflectivity profile (Fig. 18). If the reflectivity field is horizontally uniform, then on the 3.5 km horizontal cross section one should see a high reflectivity (55 dBZ)

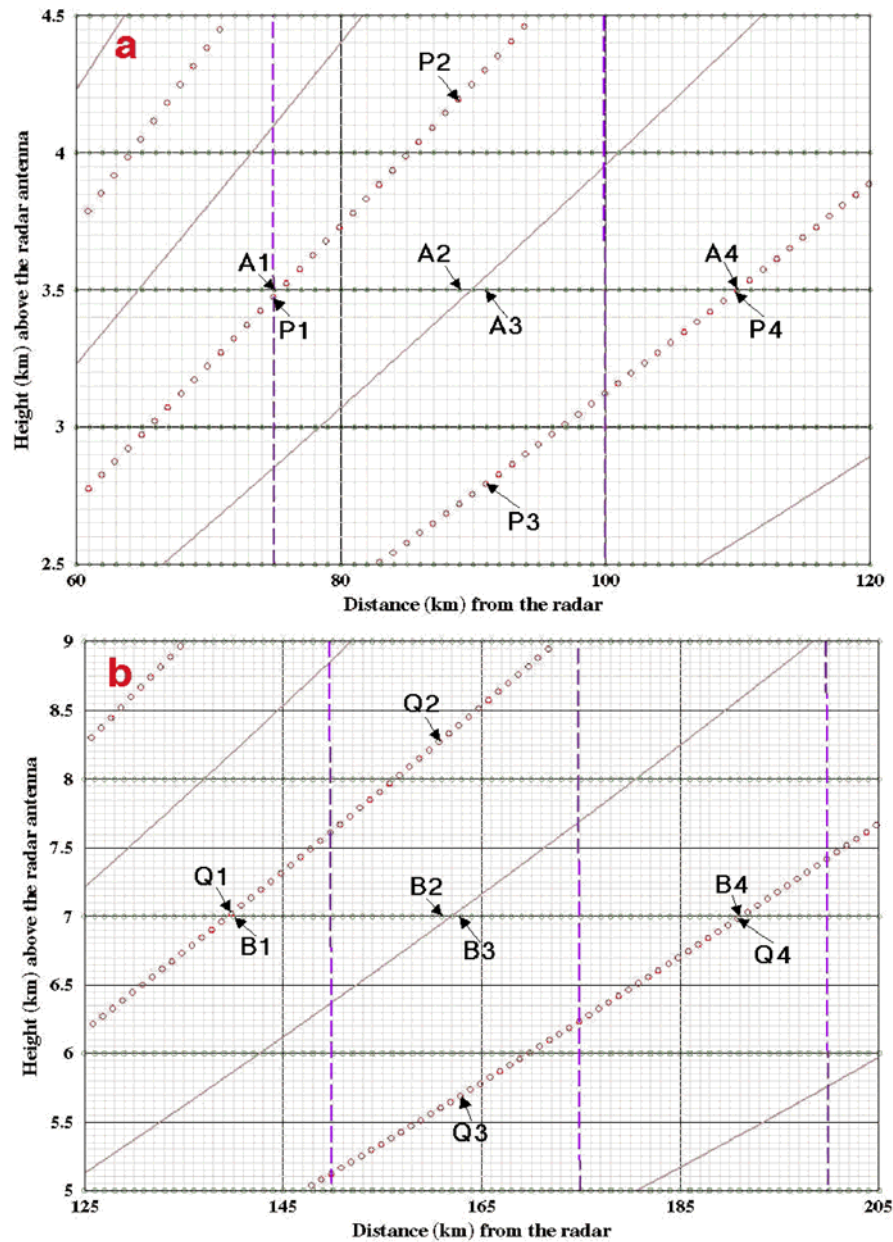


Figure 19. Vertical cross sections of radar beam geometry show the bin volume mapping process. The red circles represent centers of observed radar bins; green circles represent Cartesian grid points; purple dashed lines are range rings; and the blue and brown lines are the bottom and top of the radar beams, respectively. The range rings appear to be vertical because the horizontal scale is much larger than the vertical scale in the figure. Through the bin volume mapping scheme, A1 will get the reflectivity observation from radar bin P1, A2 from P2, A3 from P3, and A4 from P4 (panel a). Assuming a reflectivity profile as shown in Fig. 18, then A1 and A4 will get a value of ~35 dBZ while A2 gets ~22 and A3 gets ~55 dBZ. Thus on a horizontal cross section at 3.5 km height, there would be a ring-shaped discontinuity (from 22 dBZ to 55 dBZ) near 90 km range. Similarly, the Cartesian grid points B1, B2, B3, and B4 (panel b) will get values of 0, missing, 10 and 0 dBZ, respectively. And a ring of discontinuity (from missing to 10 dBZ) will appear near 160 km range on the horizontal cross-section at 7 km height.

ring at the range of A3 and a low reflectivity ring (22 dBZ) at the range of A2. Figs. 17a and 17b shows the ring problem associated with bright bands. The ring problem also happens near echo tops. Fig. 19b shows that at 7 km height, grid point B1 and B4 are collocated with centers of radar bins Q1 and Q4, respectively, so they get reflectivity value of 0 dBZ (see profile in Fig. 18). Meanwhile grid points B2 and B3 are inside radar bins Q2 and Q3 which have missing (no reflectivity signal) and ~10 dBZ, respectively. Thus on the 7 km horizontal cross section there would be a black ring (missing) at the range of B2 and a 10 dBZ ring at the range of B3. Fig. 17c shows an example of the echo top sampling problem. When reflectivity fields do not have strong vertical gradients (e.g., convective storms), then the sampling problem is much less profound (Fig. 17d).

## ii) Standard Gap Filling

To fill in the gaps in the radar sampling, extra tilts of data are generated between the adjacent observation tilts where there are large elevation angle spacings. The threshold for elevation angle spacing is  $1^\circ$  (~ beam width for the WSR-88Ds) above which extra tilts will be produced. The data on the extra tilts were obtained by horizontally interpolate the data from the two observation tilts below and above the extra tilts. Fig. 20 illustrates the gap-filling process. Suppose a gate  $g_0$  on a given gap-filling tilt is at a height of  $z_0$ . This height level intersects the two adjacent observation tilts below and above the gap-filling tilt at gates  $g_1$  and  $g_2$ , respectively. Then the reflectivity value at the gate  $g_0$  is computed by linearly interpolate between the observed reflectivities at gate  $g_1$  and  $g_2$  (Fig. 20). Listed in Table 3 are the extra tilts added for VCP 21 and VCP 11.

The gap-filling interpolation increased the horizontal influence radius for the radar bins. After the gap filling, influence radius of each data bin in the elevation angle direction is determined based on the new spacings between adjacent tilts, which are smaller than before because of the extra tilts for the gap filling. Fig. 21 shows the results obtained from the standard gap-filling scheme. The standard gap filling successfully filled in the data gaps while the ring problems still exist. To alleviate this problem, a new advanced gap-filling scheme was developed. The advanced gap-filling scheme is presented in the next section.

## iii) Advanced Gap Filling

In section a, the ring problem is shown to be caused by the poor radar sampling in vertical direction, especially in regions near the bright band, echo top, and other horizontally uniform echoes with strong vertical gradients. In these regions, reflectivity structure has much larger scale in horizontal than it is in vertical. However, radar bins have relatively fixed scale (~1km) in horizontal (approximately along range direction for low elevation angles), yet the vertical (approximately elevational direction) scale can become very large, especially at



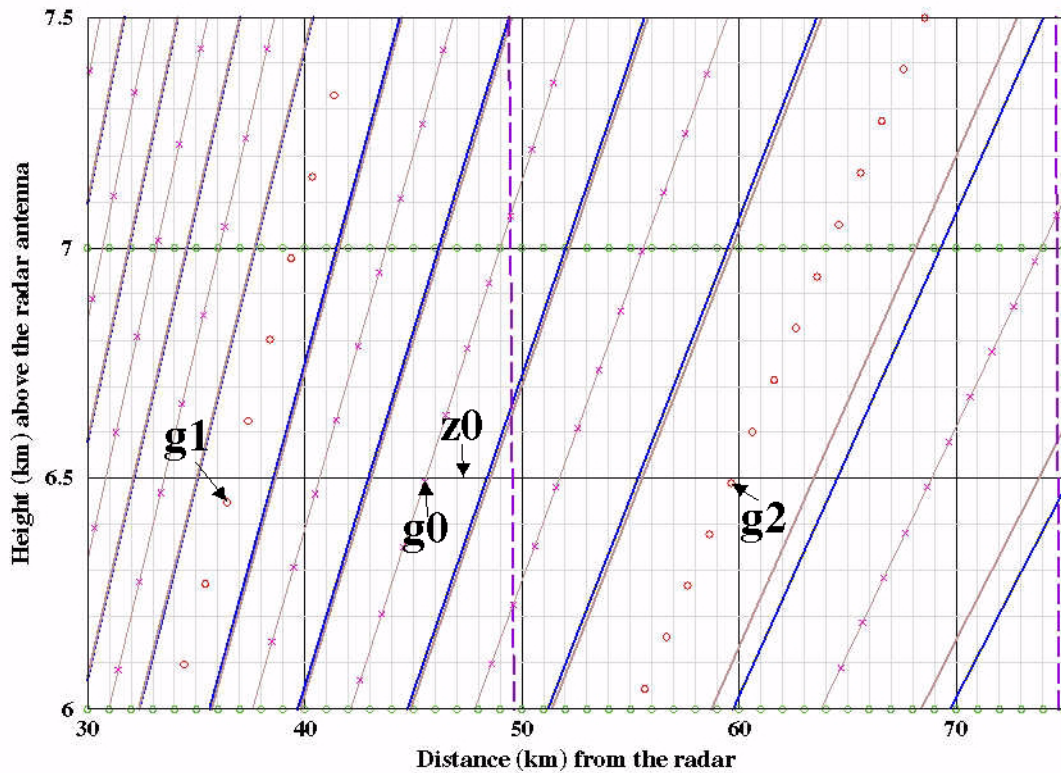


Figure 20. A schematic diagram of the standard gap-filling scheme. The symbols have the same meanings as in Fig. 19 except for that the purple “x” represents the center of bins in the gap-filling tilts. The figure shows that a gap filling bin,  $g_0$ , is at the height of  $z_0$  ( $=6.5$  km). To generate/fill a value for the bin  $g_0$ , values from two gates  $g_1$  and  $g_2$  are used. Note that  $g_1$  and  $g_2$  are the observed bins at the same height as  $g_0$ . The value at  $g_0$  was computed by linearly interpolating the two observed values at  $g_1$  and  $g_2$  using a horizontal distance-based weighting function.

**Table 3. List of the extra tilts (elevation angles in degrees) added in the standard gap-filling scheme**

VCP	Added Tilts
VCP 11	6.85°, 8.1°, 9.35°, 11.0°, 13.0°, 14.9°, 15.8°, 17.63°, 18.57°
VCP 21	5.15°, 6.975°, 7.95°, 8.925°, 10.84°, 11.78°, 12.72°, 13.66°, 15.58°, 16.56°, 17.54°, 18.52°

farther ranges. This scale discrepancy is the cause of the ring problem shown in sections a and b. To alleviate the problem, we need to increase the horizontal radius of influence and decrease the vertical radius of influence for the radar data. In the advanced gap-filling scheme, extra tilts are added not only in the data gaps, but also in regions where the radar beam become large and are farther apart in space. Table 4 shows the extra tilts generated in the advanced gap-filling scheme. The extra tilts (of data) are generated using the same method as described in the standard gap-filling scheme. Through the horizontal

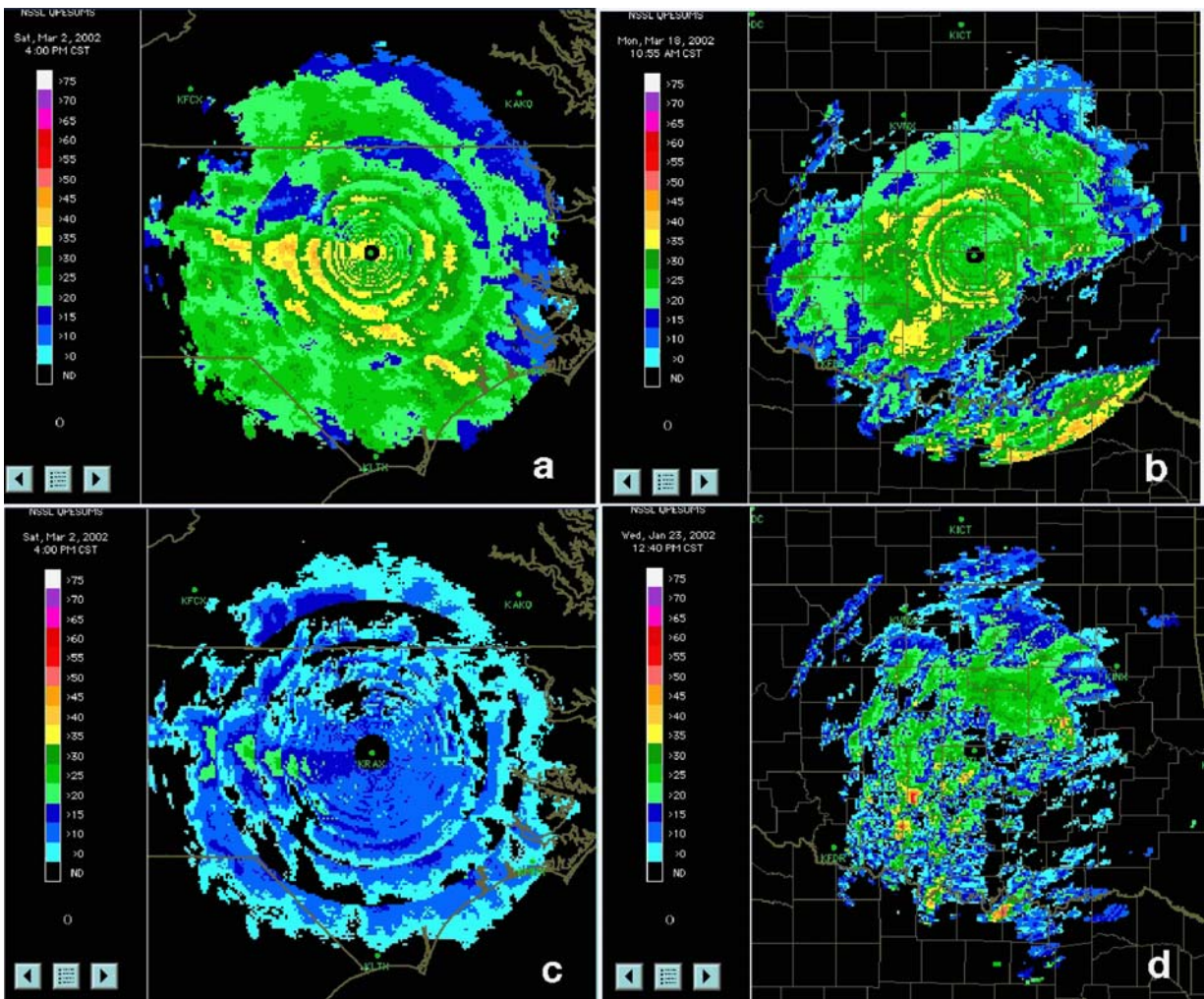


Figure 21. Results after standard gap filling.

**Table 4. List of the extra tilts (elevation angles in degrees) added in the advanced gap-filling scheme**

VCP	Added Tilts
VCP 11	1.6875°, 1.925°, 2.1625°, 2.6375°, 2.875°, 3.1125°, 3.5875°, 3.825°, 4.0625°, 4.525°, 4.75°, 4.975°, 5.53333°, 5.86667°, 6.63333°, 7.06667°, 7.9°, 8.3°, 9.13333°, 9.56667°, 10.6667°, 11.3333°, 13°, 15.35°, 18.1°
VCP 21	1.6875°, 1.925°, 2.1625°, 2.6375°, 2.875°, 3.1125°, 3.5875°, 3.825°, 4.0625°, 4.64°, 4.98°, 5.32°, 5.66°, 6.78°, 7.56°, 8.34°, 9.12°, 10.84°, 11.78°, 12.72°, 13.66°, 16.2333°, 17.8667°

interpolation the effective horizontal radius of influence is increased. The extra tilts decreased the elevational spacings between the data bins thus reduced the size of vertical influence region. The results (Fig. 22) show that the advanced



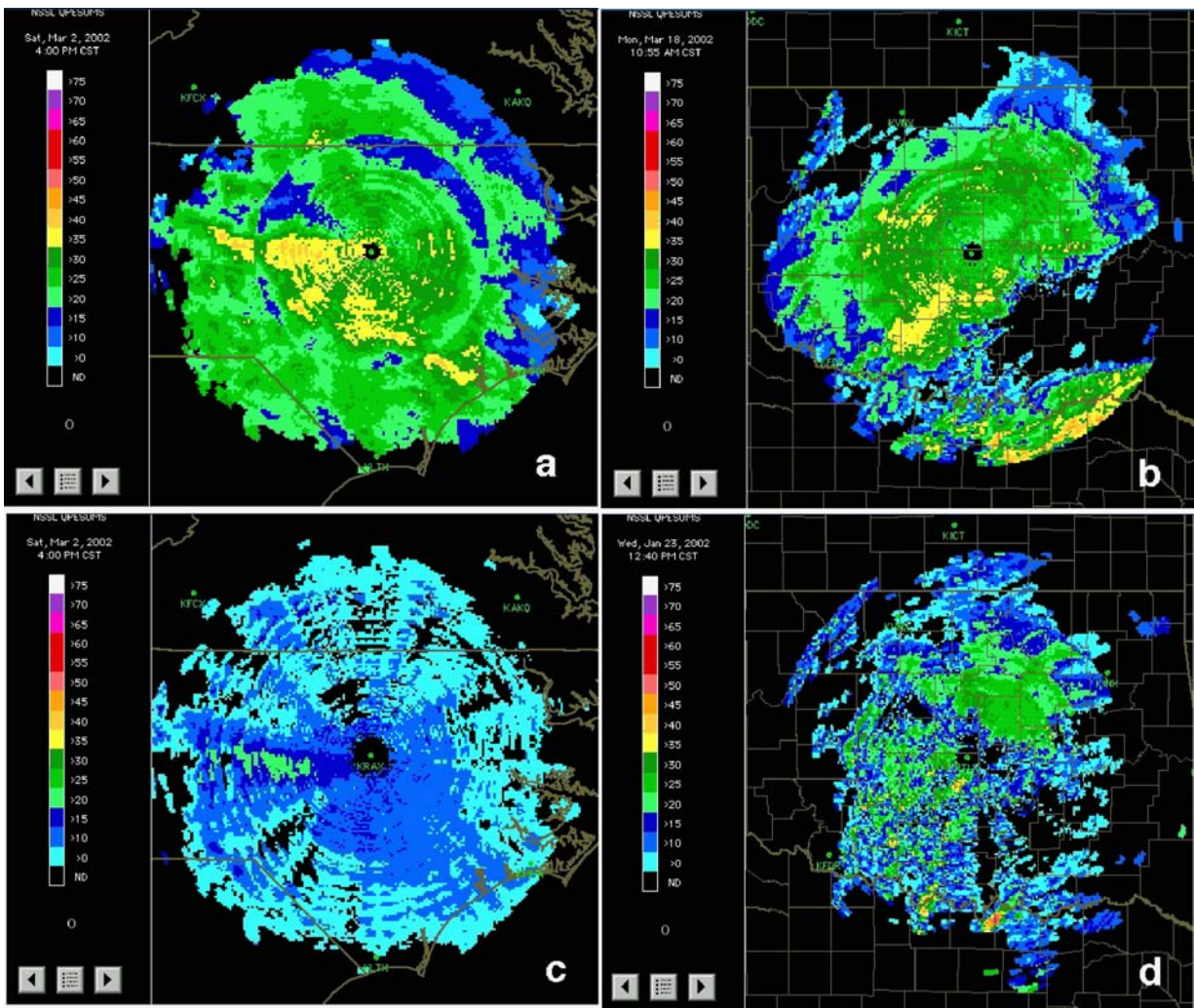


Figure 22. Results after advanced gap filling.

gap-filling technique successfully removed the ring discontinuities and produced better 3D reflectivity analyses than did the simple standard gap-filling scheme.

After a series of tests the advanced gap-filling technique is chosen to be the remapping scheme in the 3D multi-radar reflectivity mosaic. To quantitatively assess CPU usage of the 3D mosaic, three single radar cases (Table 5) are

**Table 5. Summary of the single radar precipitation cases selected for CPU benchmark testing**

Case	Grid Size (km)	Radar	VCP	% Echo Coverage
NC 1	550 × 470 × 21	KRAX	21	26.03
OK 1	600 × 400 × 21	KTLX	21	44.06
OK 2	600 × 400 × 21	KTLX	11	32.87

tested using all three gridding techniques. Table 6 summarizes the CPU usage for each case and each scheme. The advanced gap-filling scheme takes less than 20s CPU to process a volume scan with wide spread precipitation echoes (Fig. 16). The advanced gap filling was further tested for several multi-radar

**Table 6. Summary of CPU seconds used for different 3D gridding techniques and for single radar cases**

Step	NC 1	OK 1	OK 2
Radar bin volume mapping	11.11	10.95	10.53
Standard gap filling	12.18	11.83	10.98
Advanced gap filling	17.21	17.79	16.34

mosaic cases (Table 7). Among them the NC\_2 case had 6 radars, and more than 75% of precipitation coverage (Fig. 23) in North Carolina and the vicinity area. The 3D mosaic took less than 1 minute to run this case. This is very encouraging because it shows that the high resolution, high quality 3D radar analyses can be available in real-time with rapid update cycles that will meet the needs of aviation controls and management.

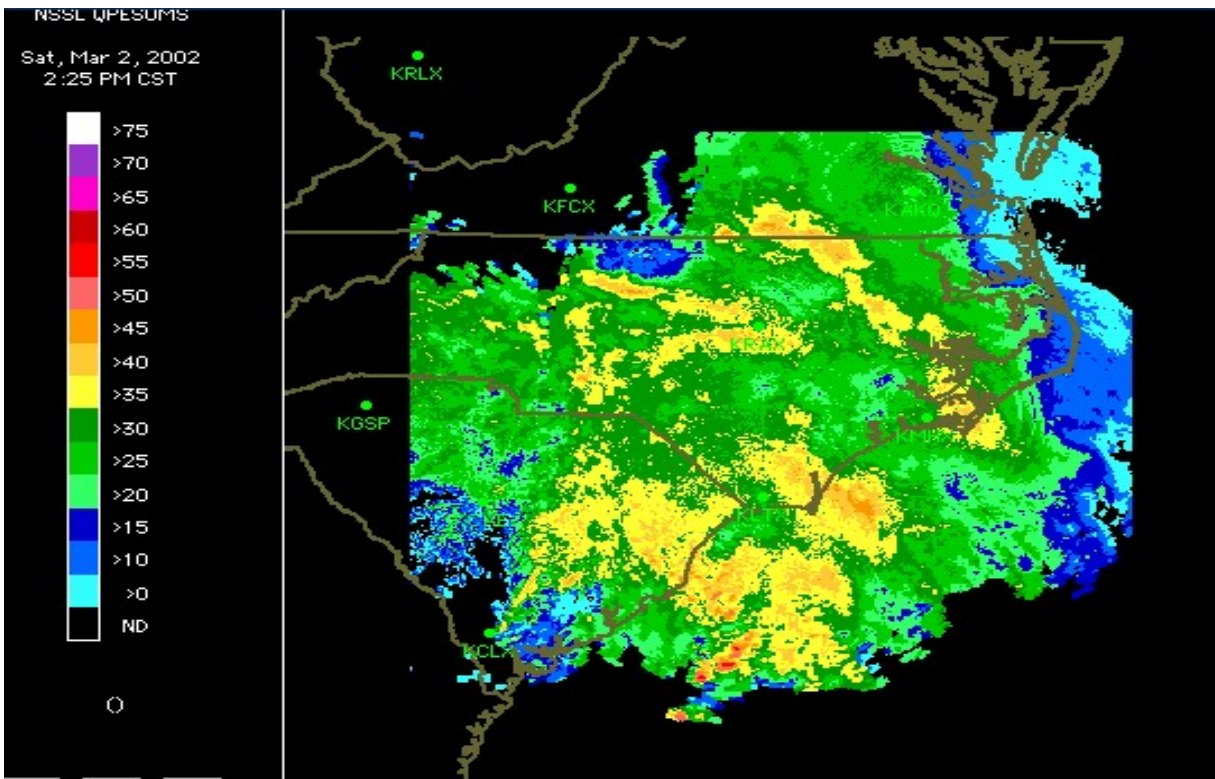


Figure 23. Composite reflectivity for the NC 2 case.

**Table 7. Summary of 3D mosaic tests using the advanced gap-filling scheme. Case IDs “CIWS A”, “CIWS B”, and “CIWS C” represent the three CIWS tile domains (see the NEPDT 1st quarter report for year 2002, task 02.6.14). All CIWS domains have the same grid size of  $480 \times 640 \times 21$  km.**

Case	Radars	VCPs	Echo Coverage (%)	CPU (s)
CIWS A1	KLOT, KIWX, KIND, KILX, KLVX, KILN	21, 21, 11, 21, 11, 11	36.89	49.09
CIWS A2	KIWX, KIND	21, 21	34.30	25.19
CIWS B1	KIND, KLVX, KILN	11, 11, 11	10.55	16.90
CIWS B2	KCLE, KPBZ, KLWX, KIND, KAKQ	21, 21, 21, 21, 21	40.15	34.91
CIWS C1	KBUF, KLWX, KAKQ	31, 21, 21	13.79	19.78
NC 2	KCAE, KAKQ, KGSP, KLTx, KMHX, KRAX	11, 21, 21, 21, 21, 21	75.23	54.96
OK 3	KAMA, KLBB, KINX, KFWS, KSRX, KTLX	31, 21, 21, 11, 21, 21	62.38	46.83

**02.6.14.5 FINAL REPORT.** The activities for the current quarter include gathering archived level-II data for 4 cases in the CIWS domain. The cases are summarized in Table 8. Three tile domains have been set up for running the 3-D

**Table 8. Summary of the precipitation cases selected for the mosaic product testing**

Case	Date	Radars
1	Dec. 13 –14, 2000	KPBZ, KLWX, KIWX, KILX, KIND, KCLE, KBUF, KAKQ
2	Aug. 18 – 19, 2001	KLVX, KLOT, KIWX, KILX, KIND, KILN, KCLE
3	Jan. 29 – 31, 2001	KBUF, KCLE, KDTX, KIWX, KILN, KLOT
4	May 31– June 2, 2001	KBUF, KCLE, KDTX, KIWX, KILN, KLOT, KPBZ

multi-radar reflectivity mosaic for the CIWS domain (see Q1 report for task 02.6.14) and Table 9 shows the domain parameters. Reference data sets including topography, spherical-to-Cartesian and Cartesian-to-spherical coordinates transformation matrixes for each radars and for each VCP modes have been generated for the three tiles.

**Table 9. Domain parameters for the three tiles that will be running the 3-D multi-radar reflectivity mosaic in real-time**

Case ID	Center lat/lon	# Grid Cells	Grid Cell Size
CIWS A	41°N, 87°W	480 × 640	0.0125°×0.0125°
CIWS B	41°N, 81°W	480 × 640	0.0125°×0.0125°
CIWS C	41°N, 75°W	480 × 640	0.0125°×0.0125°

The 3D multi-radar reflectivity mosaic algorithm was run for the first two cases at various time levels and a suite of products were generated for each time level. There are two types of products: one is in an internal binary format and the other in the NIDS raster image format. The binary products are full resolution data files including 3D reflectivity mosaic field, the composite reflectivity (i.e., the maximum reflectivity in each grid column) and the height of the composite reflectivity. These data can be used for various studies including severe storm identification and tracking, quantitative precipitation estimation, data assimilation for convective scale models, and so on. It is noteworthy that the binary file format will be changed or supplemented with NetCDF format in the near future. Using NetCDF format will speedup ingest of the mosaic products into other software and algorithms, thus increase the usefulness of the 3D mosaic data grids.

The NIDS raster products include composite reflectivity, height of the composite reflectivity and horizontal cross sections of the 3D reflectivity mosaic field on



twenty-one height levels (1, 1.5, 2, 2.5, 3, 3.5, 4, 4.5, 5, 6, 7, 8, 9, 10, 11, 12, 13, 14, 15, 16, and 17 km msl) and nine temperature surfaces (20, 10, 0, -10, -20, -30, -40, -50, and -60 °C). The temperature surfaces are obtained from the RUC2 analysis every hour. The NIDS raster data can be viewed in a web-based display system. The system has an intuitive user interface and can display the products very efficiently. These NIDS products can help air traffic controllers to visualize real-time storm systems in a regional scale and to diagnose hazardous weather situations quickly and accurately.

Figs. 24-26 show selected products for a winter storm case that occurred on

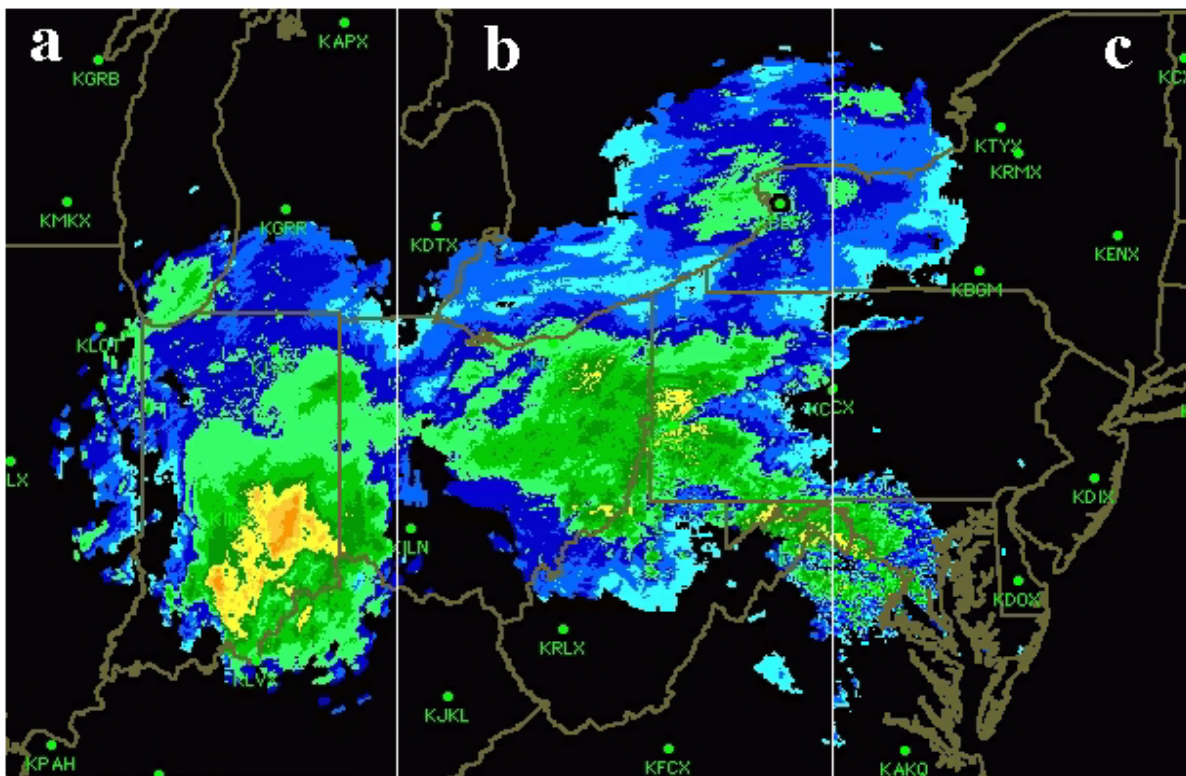


Figure 24. Composite reflectivities from the three CIWS tiles (CIWS A and CIWS B and CIWS C. See Q1 report for task 02.6.14) for a winter storm case that occurred on December 14, 2000 (0200Z). The composite reflectivity fields show seamless continuity across the boundaries between the three domains.

Dec. 14, 2000 (Case 1, Table 1) and a summer storm case that occurred on Aug. 19, 2001 (Case 2, Table 1). The results show that the 3D multi-radar mosaic scheme can generate seamless composite products for the three tiles. More importantly, the mosaic takes less than 1 minute typically to process 3-6 radars for each domain (see Table 7 in the same Q2 report for task 01.6.14.1). On the average it takes the mosaic less than 10 seconds to process one volume scan. These results are very promising since the 3D mosaic is providing regional analysis using the full resolution base level data. The tests indicate that the multi-radar mosaic algorithm can provide high-resolution and high quality

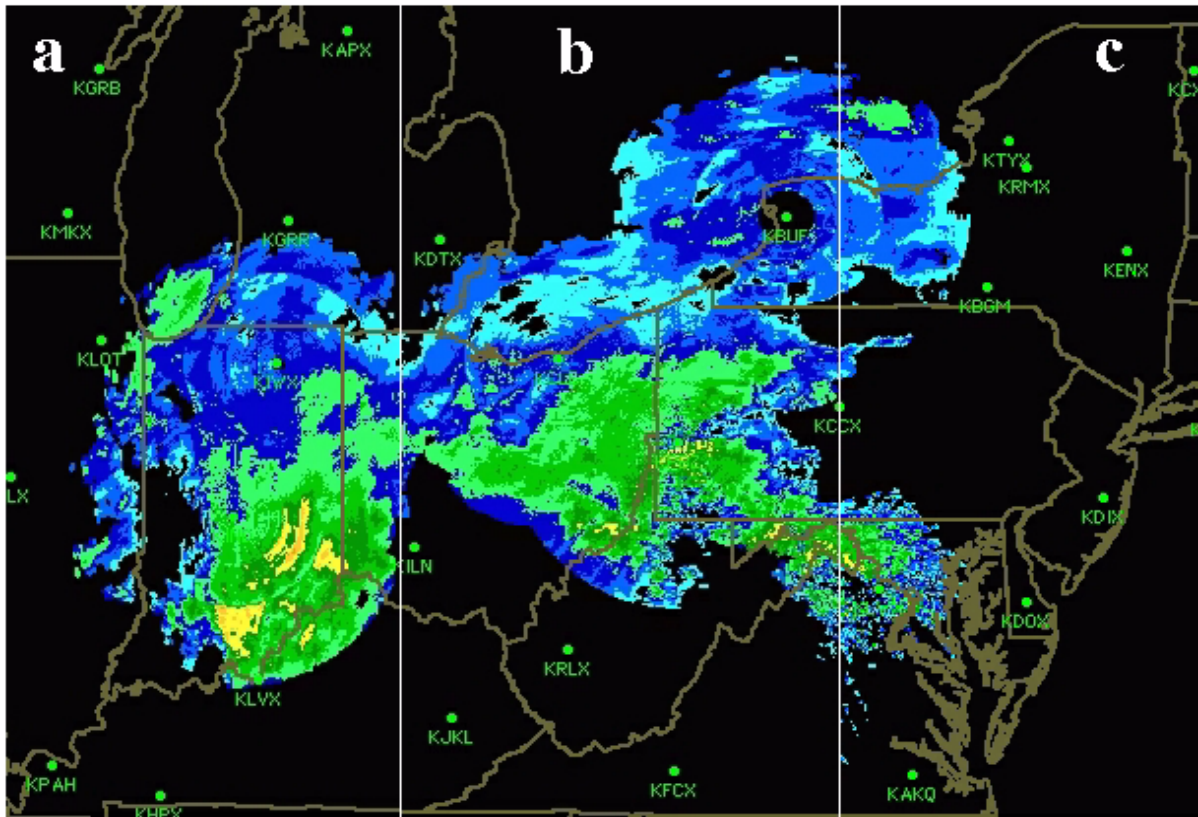


Figure 25. Same as in Fig. 24 except for horizontal cross sections of the mosaicked reflectivity field at 2.5 km msl.

3D reflectivity mosaic for ARTCC areas with very rapid update cycle. And it can be very useful for en route weather monitoring and air traffic management if deployed in real-time.

#### b) Planned Efforts

Develop product suites in NetCDF format. Purchase computers and setup initial configurations for running the 3D mosaic in real-time for the CIWS domain.

#### c) Problems/Issues

None.

#### d) Interface with other Organizations

None.

#### e) Activity Schedule Changes

None.





## 02.6.15 WARP Activities

*Develop strategies and algorithms to remove meteorologically insignificant artifacts; develop next-generation WARP products, based on multi-radar gridded data, suitable for display to air traffic controllers.*

### a) Current Efforts

NSSL is developing a quantitative verification package to evaluate the Unisys AP mitigation software. Investigation of current state-of-the-art AP/GC schemes has shown that very little quantitative evaluation is being used to critique such techniques. The quantitative verification scheme used by NSSL will be based on a method developed at MIT/Lincoln Lab. Their evaluation criteria determine the percentage of AP data that is undiagnosed and percentage of precipitation data that is incorrectly identified as AP data.

MIT/LL uses Probability of Editing Anomalous Propagation (PEAP) and Probability of Editing Weather (PEAW) as performance metrics. PEAP is given by the number of AP pixels correctly edited divided by the total number of AP pixels. PEW is given by the number of weather pixels edited divided by the total number of weather pixels. The goal is to obtain a high PEAP and a low PEW.

How to efficiently discriminate between AP and precipitation for the purpose of establishing "truth" has posed a considerable process. The process must be independent from AP identification AP by the Unisys software. Hence, meteorologists at NSSL will examine the data before seeing the Unisys output during the process.

The first two data sets to be examined are:

- 1) Amarillo, TX - 5/24/1995
- 2) St. Louis, MO - 7/3/1997.

Both cases have been previously examined and documented in other AP mitigation studies (Robinson et al., 2001) and so will provide a good calibration procedure for the NSSL meteorologists.

### References

Robinson, Michael, M. Steiner, D. B. Wolff, C. Kessinger, and R.A. Fulton, 2001: Radar Data Quality Control: Evaluation of several algorithms based on accumulating rainfall statistics. *Preprints 30th International Conference on Radar Meteorology*, Munich, P7.6.

### b) Planned Efforts

Continue progress with truthing process.

c) Problems/Issues

None.

d) Interface with other Organizations

None.

e) Activity Schedule Changes

None.

# MONITORING DROP-SIZE DISTRIBUTIONS WITH POLARIMETRIC RADAR

Edward A. Brandes<sup>1</sup>, Guifu Zhang, and J. Vivekanandan

National Center for Atmospheric Research  
Research Applications Program  
Boulder, Colorado

## 1. INTRODUCTION

Dual-polarization radars typically transmit horizontally and vertically polarized electromagnetic waves and receive backscattered signals. Because illuminated hydrometeors are not exactly spherical and not similarly oriented, their radar backscatter cross-sections are not the same for the different polarizations. Waves propagating through precipitation are subject to scattering, differential attenuation, differential phase shifts, and depolarization. Signal properties change continuously as the waves propagate yielding information that can be used to estimate particle size, shape, orientation, and thermodynamic phase. The measurements can be used to estimate the governing parameters of gamma drop-size distributions (Ulbrich 1983) and associated rainfall rates. The retrieval technique described here, an adaptation of that proposed by Zhang et al. (2001), is based on measurements of radar reflectivity at horizontal polarization and differential reflectivity and an empirical constraining relationship between the drop-size distribution (DSD) shape factor and slope parameter.

## 2. DSD RETRIEVAL METHOD

It is assumed that raindrops are represented by the gamma size distribution

$$N(D) = N_0 D^\mu \exp(-\Lambda D) \quad (1)$$

where  $N_0$  ( $\text{mm}^{-1} \text{m}^{-3}$ ) is a number concentration parameter,  $\mu$  is a distribution shape parameter, and  $\Lambda$  ( $\text{mm}^{-1}$ ) is a slope term. Note that the DSD

is described by three parameters and that their determination requires three measurements or relationships. Radar reflectivity, differential reflectivity, and specific differential phase are all related to rain rate; but for several reasons the specific differential phase is deemed a poor choice for closing the system. Instead, we close the system with a constraining relation between  $\mu$  and  $\Lambda$  and the radar reflectivity and differential reflectivity measurements. The radar reflectivities at horizontal and vertical polarization are given by

$$Z_{H,V} = \frac{4\lambda^4}{\pi^4 |K_w|^2} N_0 \int_0^{D_{\max}} D^\mu \exp(-\Lambda D) [(1 - 2\sigma_\phi^2) |f_{a,b}(D)|^2 + 2\sigma_\phi^2 |f_a(D)f_b(D)|] dD \quad (2)$$

where H and V indicate horizontal and vertical polarization states,  $\lambda$  is the radar wavelength,  $K_w$  is the dielectric factor for water,  $f_a$  and  $f_b$  are backscattering amplitudes along the major (a) and minor (b) drop axis, and  $\sigma_\phi$  is the standard deviation of the drop distribution canting angle. In the absence of information regarding drop canting, we assume for this study that  $\sigma_\phi = 0^\circ$ . The differential reflectivity is defined as the ratio of reflectivity at horizontal and vertical polarization when expressed in  $\text{mm}^6 \text{m}^{-3}$

$$Z_{DR} = \frac{Z_H}{Z_V} \quad (3)$$

Another relation is needed to compute the three parameters in (1). The procedure makes use of the correlation between  $\mu$  and  $\Lambda$ . The relationship for disdrometer observations made in Florida and having drop counts greater than  $1000 \text{ min}^{-1}$  and rain rates greater than  $5 \text{ mm h}^{-1}$  is shown in Fig. 1. The fitted empirical relation is

$$\Lambda = 1.935 + 0.735\mu + 0.0365\mu^2 \quad (4)$$

<sup>1</sup>Corresponding author address: Dr. Edward A. Brandes, National Center for Atmospheric Research, P.O. Box 3000, Boulder, CO 80307, E-mail: brandes@ucar.edu

It has been argued that relations between DSD governing parameters such as Eq. (4) could be due to statistical error in the estimated moments of the DSD. Our analysis (Zhang et al. 2002) shows that errors in the moments cause a linear relation between  $\mu$  and  $\Lambda$  and not the curvature seen in Fig. 1. Consequently, we believe the relation captures the behavior of natural DSDs.

A useful parameter is the median volume diameter ( $D_0$ ) defined as

$$\int_0^{D_0} D^3 N(D) dD = \int_{D_0}^{D_{\max}} D^3 N(D) dD$$

where  $D_{\max}$  (mm) is the equivalent volume diameter of the largest drop. One half of the liquid water content is contained in droplets smaller and one half in drops larger than  $D_0$ . A DSD parameter with more physical importance than the concentration parameter is the total drop concentration ( $N_T$ ,  $m^{-3}$ ) computed from

$$N_T = \int_0^{D_{\max}} N(D) dD.$$

The computational procedure to find the DSD parameters is to use the definition of  $Z_{DR}$  [Eq. (3)] expressed in terms of the DSD parameters and the backscattering amplitudes and Eq. (4) to retrieve  $\mu$  and  $\Lambda$  by iteration, and then use the radar reflectivity at horizontal polarization [Eq. (2)] to find  $N_0$ . The drops are assumed to have radar-apparent mean axis ratios ( $r$ ) given by (Brandes et al. 2002)

$$r = 0.9951 + 0.02510D - 0.03644D^2 + 0.005030D^3 - 0.0002492D^4$$

where  $D$  (mm) is the drop equivalent volume diameter.

For this study we estimate  $D_{\max}$  from radar reflectivity with

$$D_{\max} = 0.9468 - 0.006811Z_H + 0.004247Z_H^2 - 0.0001116Z_H^3 + 0.000001246Z_H^4 + D'$$

where  $D_{\max}$  and  $Z_H$  have units of mm and dBZ, respectively, and  $D'$  (set to 1 mm) is an adjustment to account for the likelihood that the true maximum diameter exceeds that observed. This expression was determined with disdrometer observations.

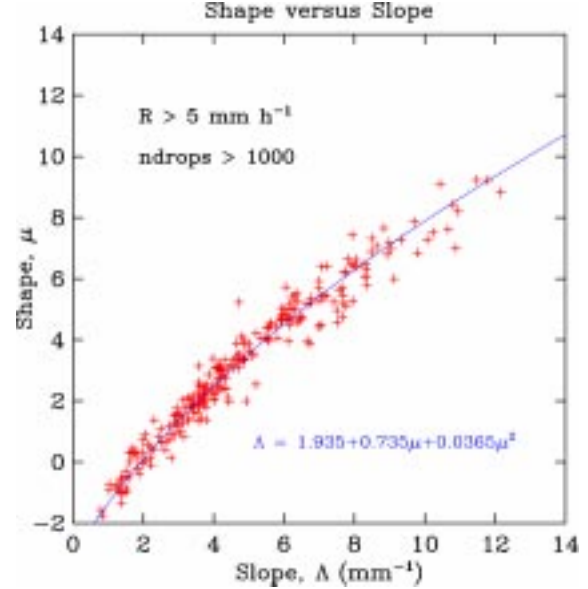


Fig. 1: The  $\mu - \Lambda$  relation for Florida DSD observations.

### 3. VERIFICATION

The constrained-gamma retrieval method was applied to S-band polarimetric radar measurements collected in Florida during the summer of 1998. One minute observations from a video disdrometer were available for comparison. The disdrometer was located 38 km from the radar. Radar measurements were made at  $0.5^\circ$  antenna elevation. The beam center was roughly 400 m above the disdrometer. Observations and computations for a long-lived event occurring on 17 September are presented in Fig. 2 and Table 1. Radar reflectivity values, as measured by radar and computed from the observed drops, are closely matched (Fig. 2a). For data points matched in time the mean difference is 0.3 dB (Table 1). Some differences are readily explained by precipitation gradients and the advection of hydrometeors. The DSD retrieval method is highly dependent on the differential reflectivity measurement. From Fig. 2b it's clear that the radar and disdrometer values are highly correlated. The mean radar and disdrometer  $Z_{DR}$ s are 0.82 and 0.84 dB, respectively.

Figures 2c and 2d present comparisons for the physical parameters  $N_T$  and  $D_0$ . The retrieval for the total drop concentration is excellent except for a few outliers and a brief period near 2100 UTC. Differences here are due to the  $N_T$  dependence on reflectivity. Using the disdrometer observations as a standard, drop concentrations are underestimated with the constrained-gamma method (Table 1). Mean logarithms of the

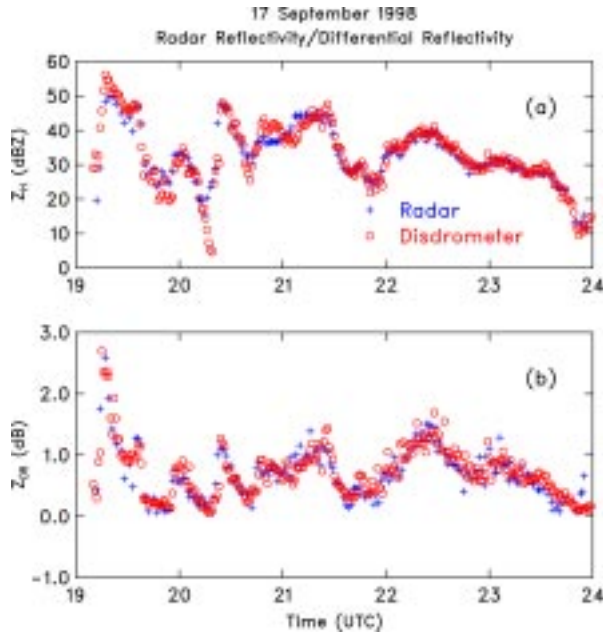


Fig. 2a,b: Radar-disdrometer plots of (a) radar reflectivity and (b) differential reflectivity.

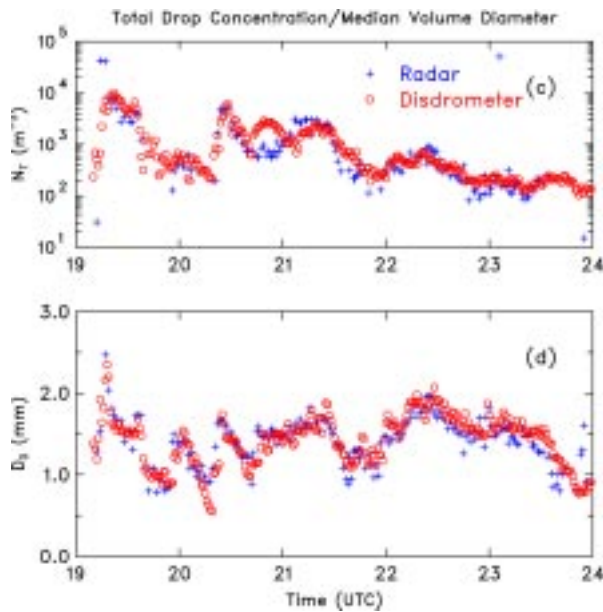


Fig. 2 continued: (c) total drop concentration and (d) median volume diameter.

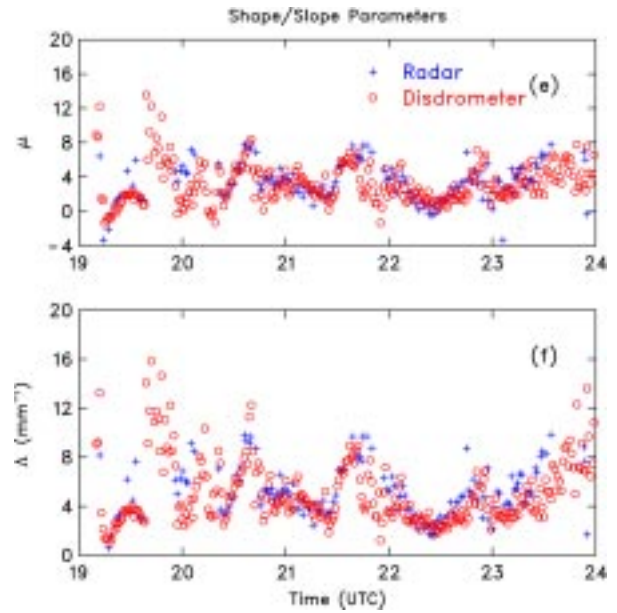


Fig. 2 continued: (e) DSD shape parameter and (f) DSD slope parameter.

concentrations differ by 0.10 (~25%). [Computations assuming that the drops are distributed exponentially ( $\mu=0$ ) yields drop concentrations that average a factor of 6 too large.] Trends in  $D_0$  are well matched. For the entire data segment estimated median drop diameters retrieved with the constrained-gamma method are 0.10 mm too large. Differences are greatest for the more convective stage of the event (1910–2130 UTC).

Gamma DSD shape and slope parameters are compared in Figs. 2e and 2f. For significant precipitation ( $Z_H \geq 25$  dBZ) trends and magnitudes show good agreement. Disdrometer-derived values tend to be less than their radar counterparts. This could be due to sample volume differences such that the disdrometer observes smaller  $D_{max}$  values than the radar. Correlations between the radar-retrieved and disdrometer-observed values are relatively low. This result stems in part from the considerable scatter and large magnitudes in the 1 min disdrometer observations at lower rain rates.

#### 4. SUMMARY AND CONCLUSIONS

The method of Zhang et al. (2001) for estimating the governing parameters of gamma drop-size distributions and rain rates from polarimetric measurements has been improved and evaluated. The three parameters of the DSD are obtained from radar reflectivity, differential

reflectivity, and a constraining empirical relation between the DSD shape factor and slope parameter. Observed trends in radar-retrieved total drop concentrations and median drop diameters showed good agreement with disdrometer observations. Agreement also was found for retrieved DSD shape and slope parameters. Differences from disdrometer-based parameters were minor and often appeared related to sampling issues in regions of precipitation gradients. The capacity of the constrained-gamma method to retrieve DSD parameters affirms the utility of the method and the enabling  $\mu - \Lambda$  relation.

Further improvement in the DSD retrievals may come from refinement of the empirical representations for radar-apparent drop shape, maximum drop size, and perhaps the raindrop distribution itself. Although trends in the retrieved DSD parameters agreed with those from the disdrometer, correlations between the one-minute samples were only moderate. Plans call for expanding this work to radar disdrometer comparisons at shorter distances to reduce sampling affects and investigating potential benefits of filtering to reduce noise levels at the lower rain rates.

*Acknowledgments.* This research is supported in large part by funds from the National Science Foundation that have been designated for the U.S. Weather Research Program at NCAR. The work also responds to requirements and funding by the Federal Aviation Administration. The views expressed are those of the authors and do not necessarily represent the official policy of the U.S. government.

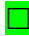


## REFERENCES

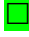
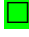


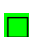

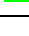


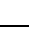
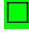



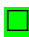

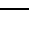

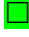
- Brandes, E. A., G. Zhang, and J. Vivekanandan, 2002: Experiments in rainfall estimation with a polarimetric radar in a subtropical environment. *J. Appl. Meteor.*, **41**, (In press).
- Ulbrich, C. W., 1983: Natural variations in the analytical form of the raindrop size distribution. *J. Climate Appl. Meteor.*, **22**, 1764-1775.
- Zhang, G., J. Vivekanandan, and E. Brandes, 2001: A method for estimating rain rate and drop size distribution from polarimetric radar measurements. *IEEE Trans. Geosci. Remote Sensing*, **39**, 830-841.
- Zhang, G., J. Vivekanandan, and E. Brandes, 2002: The shape slope relation in gamma raindrop size distributions: Statistical error or useful information? (In preparation)

Table 1: Comparison of radar reflectivity (in dBZ), differential reflectivity (dB), and DSD parameters as determined by radar and disdrometer. The units for  $D_0$  and  $\Lambda$  are mm and  $\text{mm}^{-1}$ , respectively. RMSE is the root-mean-square error. Based on 153 common data points.

	$Z_H$	$Z_{DR}$	$\log N_T$	$D_0$	$\mu$	$\Lambda$
Radar	35.3	0.82	2.74	1.53	3.4	5.0
Disdrometer	35.6	0.84	2.84	1.43	2.8	4.4
Corr. Coef.	0.94	0.81	0.81	0.61	0.48	0.52
RMSE	2.7	0.22	0.39	0.22	1.2	1.2

**Table 1: March FY 02  
Status of NEXRAD Enhancements PDT Deliverables**

**Legend:**  Task proceeding on schedule;  Task complete;  Task incomplete and overdue.

NEPDT Deliverable and Related Task	Lead Org	Due	Stat	Comment
02.6.2.1 (Polarization) HCA Development	NSSL	31/03/02		Start 01/10/01
02.6.2.2 (Polarization) Data Continuity	NSSL	31/03/02		Start 01/10/01
02.6.2.3 (Polarization) Confidence Factors	NSSL	31/03/02		Postponed
02.6.2.4 (Polarization) JPOLE Workshop	NSSL	15/06/02		Start 15/05/02
02.6.2.5 (Polarization) WSR-88D(P) Data Quality Evaluation	NSSL	30/09/02		Start 01/10/01
02.6.2.6 (Polarization) Real-Time HCA Test	NSSL	30/09/02		Start 01/10/01
02.6.2.7 (Polarization) JPOLE Phase I Data Collection, Warm Rain	NSSL	30/09/02		Start 01/04/02
02.6.2.8 (Polarization) JPOLE Phase I Data Collection: Plan Cold-Season	NSSL	30/09/02		Start 01/07/02
02.6.2.9 (Polarization) WSR-88D Cloud Tops, Thickness	NSSL	31/04/02		Start 01/10/01
02.6.2.10 (Polarization) Signal Processing to Decrease VCP Time	NSSL	30/09/02		Start 01/10/01
02.6.2.11 (Polarization) Freezing Level	NCAR	30/09/02		Start 01/10/01
02.6.2.12 (Polarization) Non-Precip HCA verification	NSSL	30/09/02		Start 01/05/02
02.6.2.13 (Polarization) Cloud Water	NCAR	30/09/02		Start 01/10/01
02.6.2.14 (Polarization) Hardware Calibration Technique	NSSL	30/09/02		Start 01/10/01
02.6.2.15 (Polarization) Sea Clutter Mitigation	NSSL	30/09/02		Start 01/10/01
02.6.3.1 (Circulation Algorithm) MDA/TDA Performance during CIWS	NSSL	30/09/02		Start 01/08/02
02.6.4.1 (Technical Facilitation) Polarization Display Development	NSSL	30/09/02		Start 30/10/01
02.6.4.2 (Technical Facilitation) WDSS-II Multi-Radar Display Development	NSSL	30/09/02		Start 01/10/01
02.6.4.3 (Technical Facilitation) WDSS-II Multi-Sensor Display Development	NSSL	30/09/02		Start 01/10/01



<b>02.6.4.4</b> (Technical Facilitation) Spectrum-Level Data QC	<b>NCAR</b>	<b>30/09/02</b>	<input type="checkbox"/>	Start 01/10/01
<b>02.6.9.1</b> (Composite Products) BBID using WSR-88D and TDWR	<b>NSSL</b>	<b>30/06/02</b>	<input type="checkbox"/>	Start 01/03/02
<b>02.6.9.2</b> (Composite Products) BBID Testing in CIWS Region	<b>NSSL</b>	<b>30/09/02</b>	<input type="checkbox"/>	Start 01/07/02
<b>02.6.11.1</b> (Volume Coverage Patterns) Data Collection	<b>NSSL</b>	<b>30/09/02</b>	<input type="checkbox"/>	Start 01/10/01
<b>02.6.12.1</b> (Product Implementation) Collaboration, Product Development	<b>NSSL</b>	<b>Quarterly</b>	<input type="checkbox"/>	Start 01/10/01
<b>02.6.14.1</b> (Multi-Radar Composites) CPU Requirements	<b>NSSL</b>	<b>31/03/02*</b>	<input checked="" type="checkbox"/>	Start 01/02/02
<b>02.6.14.2</b> (Multi-Radar Composites) Mosaic Strategies	<b>NSSL</b>	<b>30/06/02</b>	<input type="checkbox"/>	Start 01/01/02
<b>02.6.14.3</b> (Multi-Radar Composites) Real-Time Testing	<b>NSSL</b>	<b>30/09/02</b>	<input type="checkbox"/>	Start 01/07/02
<b>02.6.14.4</b> (Multi-Radar Composites) Define Analysis Domain and Grid Resolution	<b>NSSL</b>	<b>31/01/02*</b>	<input checked="" type="checkbox"/>	Start 01/10/01
<b>02.6.14.5</b> (Multi-Radar Composites) Real-Time CIWS Support	<b>NSSL</b>	<b>31/03/02*</b>	<input checked="" type="checkbox"/>	Start 12/31/01
<b>02.6.14.6</b> (Multi-Radar Composites) Display Systems	<b>NSSL</b>	<b>30/09/02</b>	<input type="checkbox"/>	Start 01/07/02
<b>02.6.15.1</b> (WARP support)Adaptable Parameter Development	<b>NSSL</b>	<b>30/06/02</b>	<input type="checkbox"/>	Start 01/10/01
<b>02.6.15.2</b> (WARP Support) Next Generation Algorithms	<b>NSSL</b>	<b>30/09/02</b>	<input type="checkbox"/>	Start 01/04/02

\* Due date revised thru AWRP POC.